

12

DNA-TR-81-11S

FINITE ELEMENT ANALYSIS OF SHOCK-INDUCED HULL CAVITATION

C. A. Felippa
J. A. DeRuntz
Lockheed Missiles & Space Company, Inc.
3251 Hanover Street
Palo Alto, California 94304

26 February 1982

Technical Report

CONTRACT No. DNA 001-81-C-0135

ADA 131271

THIS WORK WAS SPONSORED BY THE DEFENSE NUCLEAR AGENCY
UNDER RDT&E RMSS CODE B344081466 Y99QAXSF00013 H2590D.

DTIC
ELECTED
S AUG 11 1983
B

DTIC FILE COPY

Prepared for
Director
DEFENSE NUCLEAR AGENCY
Washington, DC 20305

DISTRIBUTION STATEMENT A
Approved for public release
Distribution Unlimited

83 08 .02 002

**Best
Available
Copy**

Destroy this report when it is no longer
needed. Do not return to sender.

PLEASE NOTIFY THE DEFENSE NUCLEAR AGENCY,
ATTN: STTI, WASHINGTON, D.C. 20305, IF
YOUR ADDRESS IS INCORRECT, IF YOU WISH TO
BE DELETED FROM THE DISTRIBUTION LIST, OR
IF THE ADDRESSEE IS NO LONGER EMPLOYED BY
YOUR ORGANIZATION.



UNCLASSIFIED

SECURITY CLASSIFICATION OF THIS PAGE (When Data Entered)

REPORT DOCUMENTATION PAGE		READ INSTRUCTIONS BEFORE COMPLETING FORM
1. REPORT NUMBER DNA-TR-81-119	2. GOVT ACCESSION NO. <i>A131 271</i>	3. RECIPIENT'S CATALOG NUMBER
4. TITLE (and Subtitle) FINITE ELEMENT ANALYSIS OF SHOCK-INDUCED HULL CAVITATION		5. TYPE OF REPORT & PERIOD COVERED Technical Report
7. AUTHOR(s) C. A. Felippa J. A. DeRuntz		6. PERFORMING ORG. REPORT NUMBER LMSC-D855460
9. PERFORMING ORGANIZATION NAME AND ADDRESS Lockheed Missiles & Space Company, Inc. 3251 Hanover Street Palo Alto, California 94304		8. CONTRACT OR GRANT NUMBER(s) DNA 001-81-C-0135
11. CONTROLLING OFFICE NAME AND ADDRESS Director Defense Nuclear Agency Washington, D.C. 20305		10. PROGRAM ELEMENT, PROJECT, TASK AREA & WORK UNIT NUMBERS Task Y99QAXSF-00013
14. MONITORING AGENCY NAME & ADDRESS(if different from Controlling Office)		12. REPORT DATE 26 February 1982
		13. NUMBER OF PAGES 80
		15. SECURITY CLASS. (of this report) UNCLASSIFIED
		15a. DECLASSIFICATION/DOWNGRADING SCHEDULE N/A since Unclassified
16. DISTRIBUTION STATEMENT (of this Report) Approved for public release; distribution unlimited.		
17. DISTRIBUTION STATEMENT (of the abstract entered in Block 20, if different from Report)		
18. SUPPLEMENTARY NOTES This work was sponsored by the Defense Nuclear Agency under RDT&E RMSS Code B344081466 Y99QAXSF00013 H2590D.		
19. KEY WORDS (Continue on reverse side if necessary and identify by block number) Fluid-Structure Interaction Displacement Potential Hull Cavitation Doubly Asymptotic Approximation Underwater Shock Discrete Analysis Computer Code Staggered Solution Procedure Fluid Volume Elements		
20. ABSTRACT (Continue on reverse side if necessary and identify by block number) This report describes a new version of the USA-STAGS code that can treat the problem of hull cavitation of submerged structures subjected to underwater shock. In addition, this version can also be applied to the analysis of submerged structures that include internal fluid volumes. In the present implementation, the Doubly Asymptotic Approximation (DAA) serves to simulate a radiation boundary that is located away from the fluid-structure surface at a distance sufficient to contain any cavitating region. The enclosed fluid is		

20. ABSTRACT (Continued)

cont. discretized with volume finite elements that are based upon a displacement potential formulation due to R. E. Newton. An explicit time integration method is used to advance the solution in the fluid-volume region. An implicit time integration method is still used for the structure and DAA boundary, while the staggered solution procedure has been modified to treat the interface conditions that arise from the presence of the fluid-volume elements. Results for two example problems obtained with the new software show excellent agreement with those obtained by other methods.



UNCLASSIFIED

PREFACE

The authors express their appreciation to Dr. T. L. Geers for his helpful suggestions during the course of this effort, and to Professor R. E. Newton for generating computational results for the cylindrical shell problem that were used as part of the verification of the cavitation analysis capability reported here.

Accession For	
NPS-67-001	
PC-1000	
Unpublished	
January 1968	
Hydrodynamic	
Distribution	
Available Copies	
Avail and/or	
Dist	Special
A	



TABLE OF CONTENTS

<i>Section</i>		<i>Page</i>
	PREFACE	1
	LIST OF ILLUSTRATIONS	3
I	INTRODUCTION	1-1
II	THEORY	2-1
	2.1 Problem Description	2-1
	2.2 Fluid-Volume Field Equations	2-4
	2.3 Fluid-Volume Discretization	2-7
	2.4 Time Integration	2-11
	2.5 Structure-Fluid Interaction	2-16
	2.6 Fluid-DAA Interaction	2-27
	2.7 Response Calculation Details	2-38
III	IMPLEMENTATION AND USAGE	3-1
	3.1 Implementation Overview	3-1
	3.3 Usage	3-3
IV	EXAMPLE PROBLEMS	4-1
	4.1 Overview	4-1
	4.2 Bleich-Sandler Plate Problem	4-1
	4.3 Cylindrical Shell Problem	4-6
	REFERENCES	5-1

LIST OF ILLUSTRATIONS

<i>Figure</i>		<i>Page</i>
1	Coupled-field idealization of cavitating-fluid problem	2-3
2	Stability of (2.84) for $\varphi = 0.5$ and $\alpha = 0$	2-23
3	Stability of (2.84) for $\varphi = 0.5$ and $\alpha = 1$	2-24
4	Stability of (2.84) for $\varphi = 0.5$ and $\alpha = 2$	2-25
5	Stability of (2.84) for $\varphi = 1.0$ and $\alpha = 0$	2-26
6	Non-dimensional upward velocity of plate, $\beta = 0.25$	4-3
7	Non-dimensional upward velocity of plate, $\beta = 0.50$	4-4
8	Non-dimensional upward velocity of plate, $\beta = 1.00$	4-5
9	Radial displacement of cylindrical shell, $\theta = 0^\circ$	4-9
10	Radial displacement of cylindrical shell, $\theta = 90^\circ$	4-10
11	Radial displacement of cylindrical shell, $\theta = 180^\circ$	4-11
12	Radial velocity of cylindrical shell, $\theta = 0^\circ$	4-12
13	Radial velocity of cylindrical shell, $\theta = 90^\circ$	4-13
14	Radial velocity of cylindrical shell, $\theta = 180^\circ$	4-14
15	Total pressure on cylindrical shell, $\theta = 0^\circ$	4-15
16	Total pressure on cylindrical shell, $\theta = 90^\circ$	4-16
17	Total pressure on cylindrical shell, $\theta = 180^\circ$	4-17
18	Map of cavitation zone at $t = 8$ ms, DPLPOT	4-18
19	Map of cavitation zone at $t = 8$ ms, USA-STAGS-CFA	4-19

Section I

INTRODUCTION

The USA-STAGS code [1] computes the transient response of a submerged structure that is subject to underwater shock excitation. The structural behavior may be linear or nonlinear. The success of this code in treating the complex phenomena involved is largely due to the development of the Doubly Asymptotic Approximations [2,3] that describe the fluid-structure interaction in terms of variables at the "wet" surface of the structure only, thus avoiding the modeling and computational burden produced by surrounding the structure with fluid-volume elements. This approach has opened the way to greater understanding of the problem area through computer simulation. A restricted class of problems exist, however, for which the possible effects of *hull cavitation* on the structural response must be considered. A related question concerns the treatment of *internal fluids* contained within ballast tanks, free-flooded areas, etc. An extension of the present underwater-shock computational technology to include fluid-volume elements is required to treat both of these complications.

A highly efficient computational scheme for treating a cavitating acoustic fluid has been devised by Newton [4]. The scheme involves the use of the displacement potential, which is a *scalar* quantity, as the primary variable in the formulation of finite-element matrix equations for the fluid volume. This choice has significant advantages over a displacement *vector* formulation, which triples the number of fluid-volume unknowns and does not automatically enforce irrotationality of fluid motions. A second feature of Newton's scheme is the use of an *explicit* time integra-

tion method. These two concepts form the basis of the newly constructed Cavitating Fluid Analyzer (CFA) that has been interfaced with USA-STAGS.

The theory behind the implementation of CFA and its interaction with both USA and STAGS is presented in Section II, along with stability analyses of the staggered time-integration procedure used in the coupled USA-STAGS-CFA system. Section III contains a brief discussion of the software implementation and usage of this system. Finally, Section IV presents computational results for two simple cavitation problems for which solutions are available, namely, the one-dimensional Bleich-Sandler flat-plate problem [5], and a variant of a two-dimensional cylindrical-shell problem studied by Newton [6]. The USA-STAGS-CFA results are shown to be in excellent agreement with the previous solutions.

It should be emphasized that this report is *not* a users manual for the USA-STAGS-CFA system. Such a manual will be issued once the new software has undergone further evaluation in actual three-dimensional problems and has been provided with a CFA user interface that meets the production-level needs of the underwater shock community.

Section II

THEORY

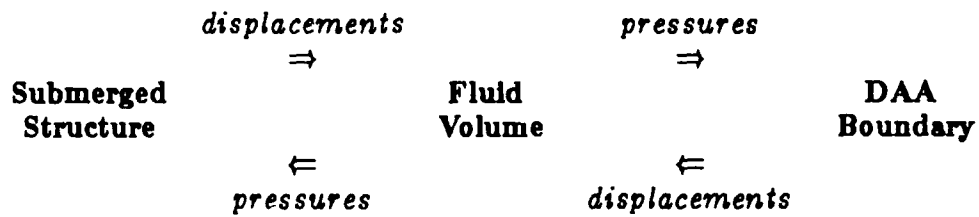
§2.1 Problem Description

A structure is submerged in a fluid idealized as an infinite acoustic medium incapable of transmitting tensile stresses. A compressive shock wave propagates through the fluid and impinges on the structure. If the structure is sufficiently flexible and the ambient hydrostatic pressure sufficiently low, the scattered negative pressure wave may induce cavitation in the subregion that was traversed by the incident shock wave before reaching the structure. This phenomenon is known as *hull cavitation*.

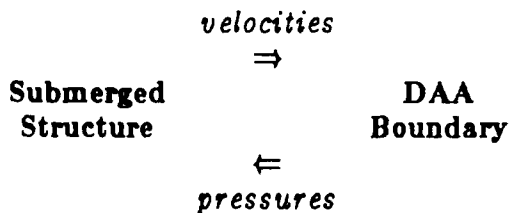
Because of the nonlinear nature of cavitation, a boundary-element treatment of the entire fluid domain as a "DAA membrane" surrounding the structure is ruled out. (Boundary element methods are restricted to homogeneous linear domains.) Instead, a realistic computer analysis of this problem requires the consideration of the three interacting fields illustrated in Figure 1: structure S , cavitating fluid volume V , and DAA membrane D .

The DAA boundary should be placed as far away as necessary to encompass the cavitating fluid subregion. Inasmuch as the extent of the latter is generally unknown before the analysis is performed, some iterations on the placement of the DAA boundary may be necessary. For example, if an analysis shows cavitation occurring at points on the DAA boundary, the latter should be moved further away from the structure interface. Conversely, if a preliminary analysis shows that wide external fluid regions remain pressurized, the DAA boundary might be moved closer to the structure to reduce the computational cost.

The nature of the interaction among the three fields (S , V , D) can be pictorially illustrated as follows.



This diagram shows that the fluid volume basically functions as a *pressure transducer* between the DAA boundary and the submerged structure. By way of contrast, the more conventional two-field structure-DAA interaction can be diagrammed as



This section presents theoretical background material with emphasis on the finite element discretization of the fluid-volume subsystem and the treatment of the coupled problem with a staggered time-integration procedure.

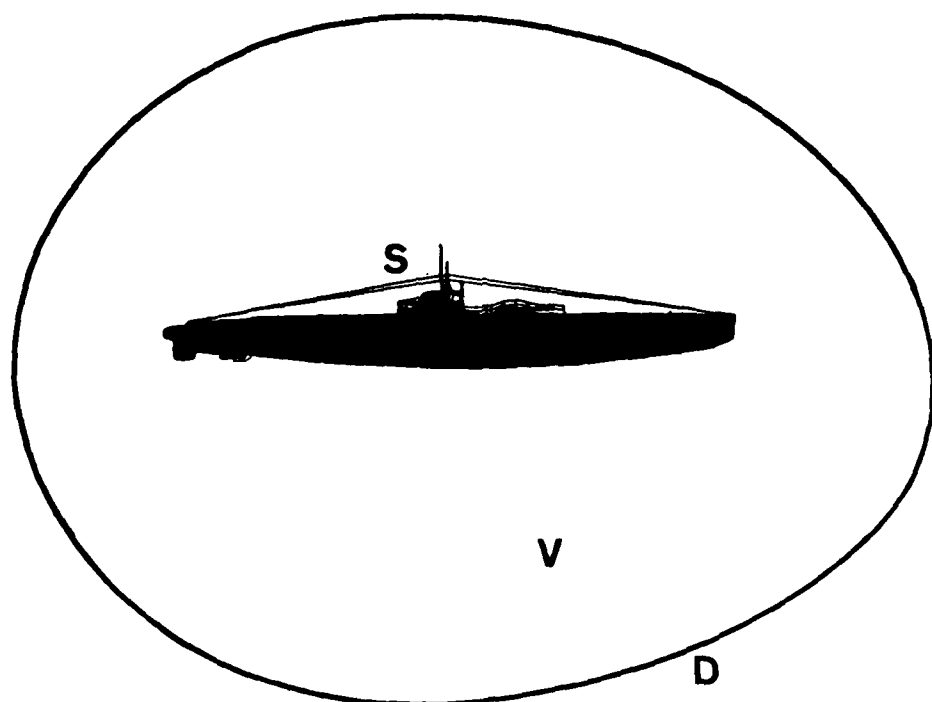


Figure 1. Coupled-field idealization of cavitating fluid problem

§2.2 Fluid-Volume Field Equations

This subsection is a compendium of well known continuous field equations for linear and bilinear acoustic fluids. These equations are collected here to introduce notation and to make this report reasonably self-contained.

Small, Irrotational Motions of a Compressible Fluid. Let p^H and ρ be the hydrostatic pressure and fluid density, respectively, in the acoustic fluid that occupies the volume V of Figure 1. Compressive pressures are conventionally denoted as *positive*. Material points in V are identified by the global-coordinate vector $\vec{X} = (X, Y, Z)$. If $\vec{f} = \vec{f}(\vec{X})$ is the body force field, then the *static equilibrium* vector equation is

$$\vec{\nabla} p^H + \vec{f} = \vec{0}. \quad (2.1)$$

Let $\vec{x} = \vec{x}(\vec{X})$ be the fluid-particle displacement field under dynamic conditions. Then

$$\vec{d} = \vec{x} - \vec{x}^H, \quad (2.2)$$

is the fluid particle displacement *relative* to a reference hydrostatic displacement \vec{x}^H . The *dynamic* vector equation of motion is

$$\rho \ddot{\vec{d}} = \vec{\nabla} p + \vec{f}, \quad (2.3)$$

where p is the total pressure.

For small irrotational fluid motions, the field \vec{d} is derivable from the scalar *displacement potential* Ψ defined by

$$\vec{\nabla} \Psi = -\rho \vec{d}. \quad (2.4)$$

The factor ρ is introduced in the potential definition for notational convenience.

$$\vec{\nabla} \ddot{\Psi} = \vec{\nabla}(p - p^H). \quad (2.5)$$

which can be spatially integrated to yield

$$\ddot{\Psi} = p - p^H, \quad (2.6)$$

For future use, define the "densified" relative condensation as

$$s = -\rho \vec{\nabla} \vec{d}. \quad (2.7)$$

From (2.4) and (2.7) it follows that

$$s = \nabla^2 \Psi. \quad (2.8)$$

Linear Fluid. The constitutive equation of a linear acoustic fluid, valid for $s \ll \rho$, is

$$p - p^H = c^2 s. \quad (2.9)$$

Here, c is the reference sound speed, which is linked to the bulk modulus K and density ρ by the relation $c^2 = K/\rho$.

Bilinear Fluid. In real fluids, cavitation is a microscopically heterogeneous phenomenon influenced by gas dilution concentrations. A simple yet effective mathematical model for this phenomenon consists of assuming that the cavitating region is *macroscopically homogeneous* and at zero total pressure. This leads to the notion of a *bilinear fluid*, whose constitutive properties are adjusted so that it cannot transmit negative total pressures. The constitutive equation of the bilinear fluid is

$$p = p^H + c^2 s \quad \text{if } s > -p^H/c^2,$$

$$p = 0 \quad \text{otherwise.} \quad (2.10)$$

The equation of motion (2.6) becomes

$$\begin{aligned}\ddot{\Psi} &= p - p^H \quad \text{if } s > -p^H/c^2, \\ \ddot{\Psi} &= -p^H \quad \text{otherwise.}\end{aligned}\tag{2.11}$$

Remark 1. Temporal differentiation of (2.4) furnishes the velocity potential equation

$$\vec{\nabla} \dot{\Psi} = -\rho \vec{u},\tag{2.12}$$

where $\vec{u} = \dot{\vec{d}}$ is the fluid-particle velocity. However, the velocity potential is not a primary field variable in the present work. The use of Ψ as primary variable has been found [4,7] to produce temporal discontinuities that are avoided by the displacement potential formulation.

Remark 2. Elimination of p and s from (2.6), (2.8) and (2.9) shows that, for a linear fluid, Ψ satisfies the scalar wave equation

$$\ddot{\Psi} = c^2 \nabla^2 \Psi\tag{2.13}$$

and, of course, so do p and s .

§2.3 Fluid-Volume Discretization

Acoustic Finite Elements. The volume V occupied by the cavitating fluid is divided into three-dimensional finite element sub-domains interconnected at element node points. The basic element used in this study is the eight-point isoparametric "brick", which is a hexahedron whose geometry is uniquely defined by the position of its eight corner points. Six-node "wedge" elements may also be used for things like rounding corners, etc.

Following standard finite element techniques, the geometry of the discretized fluid volume is expressed in the standard matrix form

$$X = \mathbf{N}^t \mathbf{X}, \quad Y = \mathbf{N}^t \mathbf{Y}, \quad Z = \mathbf{N}^t \mathbf{Z}, \quad (2.14)$$

where \mathbf{X} , \mathbf{Y} and \mathbf{Z} are column vectors of nodal values of the global coordinates $\vec{X}^t = (X, Y, Z)$, \mathbf{N} is a column vector of finite element shape functions associated with these nodes, and superscript t denotes transposition.

Matrix Equations. The displacement-potential Galerkin formulation of R. E. Newton [4,7] is used to derive the finite element matrix equations. The primary field variables of this formulation are the displacement potential Ψ and the condensation s . In accordance with the isoparametric finite element concept, these two fields are interpolated with the geometry shape functions:

$$\Psi = \mathbf{N}^t \Psi, \quad s = \mathbf{N}^t s, \quad (2.15)$$

where Ψ and s are the column vectors of node values of Ψ and s , respectively.

The discrete counterpart of the strain-displacement equation (2.8), i.e.

$$s - \nabla^2 \Psi = 0, \quad (2.16)$$

is the Galerkin equation

$$\int_V \mathbf{N} (s - \nabla^2 \Psi) dV = 0. \quad (2.17)$$

Application of the divergence theorem to (2.17) produces

$$\int_V (\mathbf{N} s + \nabla \mathbf{N} \nabla \Psi) dV = \int_B \mathbf{N} \frac{\partial \Psi}{\partial n} dB, \quad (2.18)$$

where n denotes the outward normal to the boundary B of V . Insertion of the finite element interpolation assumptions (2.15) into the left-hand side of (2.18) yields the Galerkin matrix equation

$$\mathbf{Q} \mathbf{s} = -\mathbf{H} \Psi + \mathbf{b}. \quad (2.19)$$

In this equation \mathbf{Q} and \mathbf{H} are symmetric square matrices given by

$$\mathbf{Q} = \int_V \mathbf{N} \mathbf{N}^t dV, \quad (2.20)$$

$$\mathbf{H} = \int_V (\nabla \mathbf{N}) (\nabla \mathbf{N})^t dV, \quad (2.21)$$

while the column vector \mathbf{b} is defined by

$$\mathbf{b} = \int_B \mathbf{N} \frac{\partial \Psi}{\partial n} dB. \quad (2.22)$$

The determination of the entries of \mathbf{Q} and \mathbf{H} is performed by standard numerical integration techniques for isoparametric elements, using Gauss-Legendre quadrature rules. For the time-marching calculations described in following sections, the entries of matrix

\mathbf{H} need never be explicitly calculated; instead, the vector

$$\mathbf{r} = -\mathbf{H}\Psi \quad (2.23)$$

is formed directly in the numerical integration loop.

The boundary interaction vector \mathbf{b} can be split into

$$\mathbf{b} = \mathbf{b}^s + \mathbf{b}^d, \quad (2.24)$$

where terms \mathbf{b}^s and \mathbf{b}^d come from the contributions of the structure and DAA boundary, respectively. The calculation of these terms is discussed in §2.5 and §2.6.

Dynamic Equations. The space-discrete counterpart of the field equation of motion (2.6) is

$$\ddot{\Psi} = \mathbf{p} - \mathbf{p}^H, \quad (2.25)$$

where \mathbf{p} and \mathbf{p}^H are column vectors of node values of p and p^H , respectively.

Eqs. (2.19) and (2.25) may be combined by eliminating \mathbf{p} and \mathbf{s} to yield

$$\ddot{\Psi} + c^2 \mathbf{Q}^{-1} \mathbf{H} \Psi = c^2 \mathbf{Q}^{-1} \mathbf{b}. \quad (2.26)$$

This is the finite element discretization of the wave equation (2.13) with a forcing boundary term. (This term results from the use of the divergence theorem.)

In the time integration scheme described in §2.4, the combined equation (2.26) is not used. Instead, it is far more convenient to use the two equations (2.19) and (2.25) *in tandem*, as the intermediate vector quantities \mathbf{s} and \mathbf{p} are of interest for testing the cavitation condition (1.14) and for the determination of the interface forces that act on the structure and DAA boundary.

Capacitance Lumping. Matrix \mathbf{Q} is the analog of the *consistent* capacitance (mass) matrix of finite element thermal (mechanical) models. For explicit time-marching calculations it is convenient to replace \mathbf{Q} by a “lumped capacitance” *diagonal* matrix $\tilde{\mathbf{Q}}$ to avoid solving systems of linear equations. Thus (2.19) becomes

$$\tilde{\mathbf{Q}} \mathbf{s} = -\mathbf{H} \Psi + \mathbf{b}. \quad (2.27)$$

Lumping is effected by assigning the row sums of \mathbf{Q} to the diagonal of $\tilde{\mathbf{Q}}$.

Remark 1. Some differences with Newton’s formulation as presented in Refs. [4,7] should be noted. Newton uses a displacement potential Ψ defined in terms of *total* displacements, so that the \mathbf{s} corresponding to (2.7) is the *absolute* condensation. Furthermore, he selects the opposite sign in the displacement potential definition; thus his Eqs. (2.6) and (2.8) are $\ddot{\Psi} = \mathbf{p}^H - \mathbf{p}$ and $\mathbf{s} = -\nabla^2 \Psi$, respectively.

Remark 2. Comparing (2.26) and (2.13) it is plain that $-\mathbf{Q}^{-1} \mathbf{H}$ is a discretization of the Laplacian operator ∇^2 , and so is the “lumped capacitance” form $-\tilde{\mathbf{Q}}^{-1} \mathbf{H}$. A comparison of these discrete finite element operators with conventional finite difference “molecules” is illuminating. At interior points of a regular two-dimensional mesh of square cells, $-\mathbf{Q}^{-1} \mathbf{H}$ is equivalent to the conventional 5-point “Laplacian star” finite difference molecule. On the other hand, the *lumped* form $-\tilde{\mathbf{Q}}^{-1} \mathbf{H}$ turns out to correspond to a 9-point molecule obtained by averaging two standard 5-point molecules, one being rotated by 45° . A similar but more complicated analogy holds for three dimensions.

§2.4 Time Integration

For numerical stability reasons discussed later in this and following subsections, the introduction of artificial damping terms in the fluid-volume equations of motion turns out to be highly beneficial. To simplify matters, however, we start the presentation of fluid-volume time integration techniques assuming that such terms are absent.

Undamped Integration. Equation (2.25) is numerically integrated in time with an *explicit central difference scheme*. Let $(\cdot)_n$ denote the computed value of (\cdot) at the n -th time station t_n . Computations have proceeded until t_n . If h is the time increment $t_{n+1} - t_n$, the central difference scheme can be written

$$\dot{\Psi}_{n+1/2} = \Psi_{n-1/2} + h(\mathbf{p}_n - \mathbf{p}^H), \quad (2.28)$$

$$\Psi_{n+1} = \Psi_n + h \dot{\Psi}_{n+1/2}. \quad (2.29)$$

The advancing step is completed by the discrete strain-displacement equation (2.19) and the constitutive equation (2.9):

$$\overset{2.27}{\tilde{\mathbf{Q}} \mathbf{s}_{n+1}} = -\mathbf{H} \Psi_{n+1} + \mathbf{b}_{n+1}, \quad (2.30)$$

$$\mathbf{p}_{n+1} = \mathbf{p}^H + c^2 \mathbf{s}_{n+1}. \quad (2.31)$$

Inasmuch as $\tilde{\mathbf{Q}}$ is a diagonal matrix, the solution of the linear system (2.30) for \mathbf{s}_{n+1} is trivial.

Note that in this process Ψ , \mathbf{s} and \mathbf{p} are computed at *full stations*, whereas $\dot{\Psi}$ is computed at *half stations*:

$$\begin{array}{ccccccc} \cdots & \Psi_{n-1} & \Psi_n & \Psi_{n+1} & \cdots \\ \cdots & \dot{\Psi}_{n-1/2} & \dot{\Psi}_{n+1/2} & \cdots \\ \cdots & \mathbf{p}_{n-1} & \mathbf{p}_n & \mathbf{p}_{n+1} & \cdots \end{array}$$

This has important implications in the starting procedure described in §2.7.

If the forcing vector \mathbf{b} does not depend on left-hand side variables, the numerical stability of the central difference scheme (2.26)-(2.31) is well known. It can be expressed as the Courant-Friedrichs-Levy (CFL) condition

$$h \leq h_C = L/c, \quad (2.32)$$

where L is the *smallest cross dimension* of a fluid-volume finite element; h_C is called the Courant timestep. The CFL condition (2.32) will be derived later in this section as a particular case of the damped system integration.

The accuracy properties of the central difference operator are also well known. It does not introduce numerical damping. On a regular grid of equal-side elements, integrating with $h = h_C$ furnishes exact nodal results for the propagation of plane-waves of rectangular profile (*e.g.* step-waves) along gridlines. For all other cases ($h \neq h_C$, irregular grids, or general waveforms), numerical dispersion occurs and the solution is inexact.

Artificial Damping. Newton's studies [4,7] have indicated that occurrence of cavitation can induce growing spurious pressure oscillations. These oscillations eventually cause "fragmentation" of the cavitation region in the sense that small pressurized islands appear in the cavitation region while small zero-pressure bubbles appear in the pressurized region. The phenomenon has been termed *frothing*.

The most effective cure to frothing is *numerical damping that increases with frequency*. This can be achieved by augmenting (2.25) with an artificial damping term proportional to $\$$:

$$\ddot{\Psi} = \mathbf{p} - \mathbf{p}^H + \beta hc^2 \$, \quad (2.33)$$

in which β is a dimensionless damping coefficient that varies from 0 to 1. The value of $\$$ is estimated by a backward difference formula.

For a pressurized fluid (2.33) would reduce to the slightly simpler form

$$\ddot{\Psi} = \mathbf{p} - \mathbf{p}^H + \beta h \dot{\mathbf{p}}, \quad (2.34)$$

since $\$ = \dot{\mathbf{p}}/c^2$. But the expression (2.33) is more general, as it can be used for a cavitation region in which $\dot{\mathbf{p}}$ is unrelated to $\$$.

The modified solution-advancing process, including the test for cavitation, is as follows.

$$\$_n = (\mathbf{s}_n - \mathbf{s}_{n-1})/h, \quad (2.35)$$

$$\dot{\Psi}_{n+1/2} = \dot{\Psi}_{n-1/2} + h(\mathbf{p}_n - \mathbf{p}^H + \beta h c^2 \$_n), \quad (2.36)$$

$$\Psi_{n+1} = \Psi_n + h \dot{\Psi}_{n+1/2}, \quad (2.37)$$

$$\tilde{\mathbf{Q}} \mathbf{s}_{n+1} = -\mathbf{H} \Psi_{n+1} + \mathbf{b}_{n+1}, \quad (2.38)$$

$$\mathbf{p}_{n+1} = \max(\mathbf{p}^H + c^2 \mathbf{s}_{n+1}, 0). \quad (2.39)$$

Stability of Damped Integration. The following study investigates how the stable timestep depends on the artificial damping coefficient, which is obviously a question of practical importance. The effect of structure- and DAA-coupling terms on numerical stability is ignored here. These two effects are examined in §2.5 and §2.6, respectively.

The stability analysis of the advancing process (2.35)-(2.39) is undertaken with a Fourier (normal mode) method, which involves fairly conventional steps. First, the nonhomogeneous vector terms: hydrostatic pressure \mathbf{p}'' and boundary force \mathbf{b} are discarded (the latter because of the interaction neglect as noted previously). Next, the state variables (Ψ , \mathbf{s} and \mathbf{p}) are expanded into normal-mode motions associated with the eigenproblem

$$\tilde{\mathbf{Q}} \mathbf{v} = \lambda \mathbf{H} \mathbf{v}. \quad (2.40)$$

Inasmuch as both $\tilde{\mathbf{Q}}$ and \mathbf{H} are symmetric and nonnegative definite ($\tilde{\mathbf{Q}}$ is in fact positive definite), all eigenvalues λ of (2.40) are real and positive.

The advancing step (2.35)-(2.39) is rewritten for a specific normal mode of eigenfrequency λ :

$$\dot{\psi}_{n+1/2} = \dot{\psi}_{n-1/2} + h[p_n + \beta c^2(s_n - s_{n-1})], \quad (2.41)$$

$$\psi_{n+1} = \psi_n + h\dot{\psi}_{n+1/2}, \quad (2.42)$$

$$s_{n+1} = -\lambda\psi_{n+1}, \quad (2.43)$$

$$p_{n+1} = \gamma c^2 s_{n+1} = -\gamma\lambda c^2 \psi_{n+1}. \quad (2.44)$$

In these equations, ψ , s and p denote *amplitudes* of Ψ , s and p , respectively, and γ is a *switch variable* that takes the value 1 for pressurized fluid ($p > 0$) and 0 for cavitating fluid ($p = 0$). [Implicit in the use of γ is the assumption that a normal mode pertains wholly to either condition; this can be only justified *a posteriori* by showing that only one condition is critical.]

Elimination of the three intermediate variables $\dot{\psi}$, s and p yields the difference equation

$$\psi_{n+1} - 2\psi_n + \psi_{n-1} = -\varsigma[(\gamma + \beta)\psi_n - \beta\psi_{n-1}], \quad (2.45)$$

with

$$\varsigma = h^2 c^2 \lambda, \quad (2.46)$$

which is a dimensionless parameter.

The associated characteristic polynomial in the complex amplification variable z (the discrete Laplace transform image of ψ) is

$$C(z) = z^2 - [2 - \varsigma(\gamma + \beta)]z + 1 - \varsigma\beta. \quad (2.47)$$

The corresponding Routh polynomial, obtained through the involutory mapping $z = (y + 1)/(y - 1)$, is

$$\varsigma(\gamma + \beta)y^2 + 2\varsigma\beta y + 4 - \varsigma(\gamma + 2\beta), \quad (2.48)$$

from which it is easy to deduce the stability conditions

$$h \leq \frac{2}{c\sqrt{\lambda(\gamma + 2\beta)}} \quad \text{and} \quad \beta \geq 0. \quad (2.49)$$

This expression shows that the smallest stable timestep is associated with the *largest* eigenvalue λ of (2.40). It can be shown that for trilinear shape functions λ is bounded above by $4/L^2$, where L is the smallest finite element mesh dimension. (This eigenvalue is associated with "hourglass" geometric

distortions.) Inserting this bound in (1.49) yields the desired formula

$$h \leq h_{max} = \frac{h_C}{\sqrt{\gamma + 2\beta}}, \quad (2.50)$$

where h_C is the Courant timestep defined by (2.32).

Setting $\gamma = 0$ increases the stability limit if $\beta \geq 0$. Thus *the occurrence of cavitation does not have a detrimental effect on stability*. From now on we can conservatively set $\gamma = 1$.

If $\beta = 0$, the stability limit (2.32) of the undamped central difference scheme (2.28)-(2.31) results. But if $\beta > 0$, the stability limit is *reduced* by the factor $1/\sqrt{1+2\beta}$. This factor reaches $1/\sqrt{3} = 0.577$ for $\beta = 1$, which is the maximum suggested damping.

There is in fact a slightly smaller *recommended* maximum timestep. This is the *transition* stepsize h_{tr} at which the roots of the quadratic characteristic equation $C(z) = 0$ pass from imaginary to real. Imposing the double root condition readily yields

$$h_{tr} = \frac{h_C}{1+\beta}. \quad (2.51)$$

This is smaller than h_{max} , but differs by at most 15% from it if $\beta \leq 1$, as illustrated by the following table.

β	h_{max}/h_C	h_{tr}/h_C
0.000	1.000	1.000
0.250	0.816	0.800
0.500	0.707	0.667
0.750	0.632	0.571
1.000	0.577	0.500

For plots of h/h_C vs. β , see Figures 2 through 5 in §2.5.

§2.5 Structure-Fluid Interaction

Action of Fluid-Volume on Structure. The differential equation of motion for the dynamic response of a structure spatially discretized by the finite element method can be expressed in the form

$$\mathbf{M}_s \ddot{\mathbf{x}}^s + \mathbf{C}_s \dot{\mathbf{x}}^s + \mathbf{K}_s \mathbf{x}^s = \mathbf{f}_s, \quad (2.52)$$

where \mathbf{x}^s is the column vector of nodal structure displacements, \mathbf{M}_s , \mathbf{C}_s and \mathbf{K}_s are the structural mass, damping and stiffness matrices, respectively, and \mathbf{f}_s is the external nodal force vector. For acoustic-wave excitation of a submerged structure through the fluid-volume mesh, \mathbf{f} is given by

$$\mathbf{f}_s = -\mathbf{G}_s \mathbf{A}_s \mathbf{p}, \quad (2.53)$$

where \mathbf{p} is the column vector of total pressures at the nodes of the fluid-volume mesh, as in (2.25), \mathbf{A}_s is a diagonal matrix of contributing surface areas surrounding fluid-volume nodes in contact with the structure, and \mathbf{G}_s is the transformation matrix that relates structure and fluid nodal surface forces. If the structure and fluid-volume nodes are in one-to-one correspondence, \mathbf{G}_s reduces to the identity matrix for all wet-surface structure nodes, and is zero otherwise.

Action of Structure on Fluid-Volume. The effect of the structural response on the fluid volume field resides in the boundary interaction term \mathbf{b}^s implicitly defined by (2.23) and (2.24):

$$\mathbf{b}^s = \int_{B_s} \mathbf{N} \frac{\partial \Psi}{\partial n} dB, \quad (2.54)$$

where B_s is the wet structure (contact) surface. To evaluate \mathbf{b}^s , replace

$$\frac{\partial \Psi}{\partial n} = -\rho w = \rho \vec{x}^s \vec{n}, \quad (2.55)$$

and

$$x^s = \mathbf{N}_s^t \mathbf{x}^s. \quad (2.56)$$

in (2.54). Here w is the structural displacement normal to the structure's wet surface; \vec{n} is the wet surface normal vector considered as positive going *into* the fluid, and \mathbf{N}_s is an array of normal-displacement structural shape functions. The result can be expressed as

$$\mathbf{b}^s = \rho \mathbf{L}_s \mathbf{x}^s, \quad (2.57)$$

where the matrix \mathbf{L}_s is given by

$$\mathbf{L}_s = \int_{B_s} \mathbf{N} \mathbf{N}_s^t \Gamma_s dB, \quad (2.58)$$

in which Γ_s is a diagonal matrix of normal direction cosines.

In practice, the entries of \mathbf{L}_s need not be explicitly calculated and stored. Instead, the whole process of going from vector \mathbf{x}^s to vector \mathbf{b}^s can be conveniently packaged within a numerical integration framework. The effective result of the numerical integration process can be presented in the "lumped area" form

$$\mathbf{b}^s = \rho \mathbf{A}_s \mathbf{G}_s^t \mathbf{x}^s, \quad (2.59)$$

where \mathbf{A}_s and \mathbf{G}_s are the same as in Equation (2.53).

Staggered Integration. The semi-discrete equations of motion of the two interacting fields: submerged structure and fluid volume, are numerically integrated with a *staggered solution procedure* in which only two vectors: nodal pressures \mathbf{p} and structure displacements \mathbf{x}^s , are passed back and forth between the structure and fluid-volume software modules.

The structural equations of motion (2.52) are treated by an *implicit* time integration formula, which yields a (generally non-linear) algebraic system that must be solved at each step:

$$\mathbf{E}_s \mathbf{x}_n^s = \mathbf{h}^s + \mathbf{f}_n^N + \delta^2 \mathbf{f}_n, \quad (2.60)$$

where

$$\mathbf{E}_s = \mathbf{M}_s + \delta \mathbf{C}_s + \delta^2 \mathbf{K}_s, \quad (2.61)$$

δ is an integrator-dependent generalized stepsize, \mathbf{h}^s is a term that embodies the effect of previous structural solutions, and \mathbf{f}_n^N is a nonlinear pseudo-force term.

Combining the previous equations with the artificially damped central-difference advancing step (2.35)-(2.39), the following time marching scheme results:

$$\mathbf{E}_s \mathbf{x}_n^s = \mathbf{h}_n^s + \mathbf{f}_n^N - \delta^2 \mathbf{G}_s \mathbf{A}_s \mathbf{p}_n, \quad (2.62)$$

$$\mathbf{b}_n^s = \rho \mathbf{A}_s \mathbf{G}_s^t \mathbf{x}_n^s, \quad (2.63)$$

$$\mathbf{s}_n = (\mathbf{s}_n - \mathbf{s}_{n-1})/h, \quad (2.64)$$

$$\dot{\Psi}_{n+1/2} = \dot{\Psi}_{n-1/2} + h(\mathbf{p}_n - \mathbf{p}^H + \beta h c^2 \mathbf{s}_n), \quad (2.65)$$

$$\Psi_{n+1} = \Psi_n + h \dot{\Psi}_{n+1/2}, \quad (2.66)$$

$$\tilde{\mathbf{Q}} \mathbf{s}_{n+1} = -\mathbf{H} \Psi_{n+1} + \mathbf{b}_{n+1}^s + \mathbf{b}_{n+1}^d, \quad (2.67)$$

$$\mathbf{p}_{n+1} = \max(\mathbf{p}^H + c^2 \mathbf{s}_{n+1}, 0). \quad (2.68)$$

The only undefined term in these equations is now \mathbf{b}^d , which comes from the DAA boundary interaction. This term is dealt with in §2.6.

The *simplest staggered solution procedure* for the preceding equations is obtained if one identifies \mathbf{b}_{n+1}^s with \mathbf{b}_n^s , and similarly for the solution-dependent portion of \mathbf{b}^d . The net effect of this "last solution" staggering is that the structure "lags" one step behind the fluid volume.

An obvious refinement to the previous scheme is the use of a *predictor* \mathbf{x}_n^{sP} for \mathbf{x}_{n+1}^s in (2.63) instead of simply inserting the last solution \mathbf{x}_n^s . For example,

$$\mathbf{b}_n^s = \rho \mathbf{A}_s \mathbf{G}_s^t \mathbf{x}_n^{sP} = \rho \mathbf{A}_s \mathbf{G}_n^t (\mathbf{x}_n^s + h \dot{\mathbf{x}}_n^s). \quad (2.69)$$

Predictors may be used not only to improve accuracy, but also *stability* of specific integration formulas, as shown in the following study.

Stability of Staggered Integration. The stability analysis presented here follows Fourier techniques similar to those used in §2.4. Let x be the amplitude of a structural displacement mode, and let m , a and f be the corresponding generalized mass, contact area, and pressure force, respectively. The structural damping can be neglected from the outset. The structure *stiffness* can also be ignored, as a deeper analysis (not reported here) shows. Stiffness nonlinearities can be therefore ignored. Thus only mass and contact area govern stability.

The modal structural equations will be integrated by the general one-step implicit method:

$$x_n = x_{n-1} + h[\varphi \dot{x}_n + (1 - \varphi) \dot{x}_{n-1}], \quad (2.70)$$

$$\dot{x}_n = \dot{x}_{n-1} + h[\varphi \ddot{x}_n + (1 - \varphi) \ddot{x}_{n-1}]. \quad (2.71)$$

This integrator specializes to Backward Euler for $\varphi = 1$ and to the trapezoidal rule for $\varphi = 1/2$. The generalized stepsize is $\delta = \varphi h$. For zero damping and stiffness, the implicit equation (2.60) reduces to

$$mx_n = m(x_{n-1} + h\dot{x}_{n-1}) + h^2[\varphi^2 f_n + \varphi(1 - \varphi) f_{n-1}]. \quad (2.72)$$

The assumed predictor for the interaction term is

$$x'_{n+1} = x_n + \alpha h \dot{x}_n, \quad (2.73)$$

where α is a free parameter.

As for the fluid-volume modal equations, (2.41) through (2.44) apply with only the following changes: γ is set to one (pressurized fluid, as a cavitating fluid mode maintains zero pressure and does not interact), and the structure boundary coupling term b^s is added to (2.43). This term is divided by q , which is the generalized capacitance associated with the fluid-volume mode under consideration. Here is the complete set of difference equations:

$$mx_n = m(x_{n-1} + h\dot{x}_{n-1}) - ah^2[\varphi^2 p_n + \varphi(1 - \varphi) p_{n-1}], \quad (2.74)$$

$$b_n^s = \rho a(x_n + \alpha h \dot{x}_n), \quad (2.75)$$

$$\dot{\psi}_{n+1/2} = \dot{\psi}_{n-1/2} + h[p_n + \beta c^2(s_n - s_{n-1})], \quad (2.76)$$

$$\psi_{n+1} = \psi_n + h \dot{\psi}_{n+1/2}, \quad (2.77)$$

$$s_{n+1} = -\lambda \psi_{n+1} + b_n^s/q, \quad (2.78)$$

$$p_{n+1} = c^2 s_{n+1}. \quad (2.79)$$

Elimination of the intermediate fluid variables $\dot{\psi}$, s and p furnishes two coupled difference equations:

$$\begin{aligned} \psi_{n+1} - [2 - \varsigma(1 + \beta)]\psi_n + (1 - \varsigma\beta)\psi_{n-1} = \\ (\rho ah^2 c^2 / q)[(1 + \beta)x_{n-1} - \beta x_{n-2} + \alpha(1 + \beta)h\dot{x}_{n-1} - \alpha\beta h\dot{x}_{n-2}], \end{aligned} \quad (2.80)$$

$$\begin{aligned} x_n - (1 - \varphi^2\mu)x_{n-1} + \varphi(1 - \varphi)\mu x_{n-2} - (1 - \alpha\mu)h\dot{x}_{n-1} \\ + \varphi(1 - \varphi)\alpha\mu h^2 h\dot{x}_{n-2} = \varsigma a/m[\varphi^2\psi_n + \varphi(1 - \varphi)\psi_{n-1}], \end{aligned} \quad (2.81)$$

where ς is given by (2.46), and

$$\mu = \frac{\rho a^2 c^2 h^2}{mq}, \quad (2.82)$$

is a dimensionless parameter that measures the strength of fluid-structure modal coupling.

Direct elimination of the velocity terms in the preceding equations is messy. It is more convenient to pass to the transform space z first, and then eliminate them through the operator relation

$$h\dot{x}_k = \frac{z - 1}{\varphi z + 1 - \varphi} x_k, \quad k = n, n - 1, \dots \quad (2.83)$$

which follows from σ -transforming (2.70). The resulting characteristic polynomial can be expressed as

$$\check{C}(z) = C_{ff}(z) C_{ss}(z) - \mu \varsigma C_{sf}(z) C_{fs}(z), \quad (2.84)$$

where

$$\begin{aligned} C_{ss}(z) = z^3 + [-2 + (\varphi^2 + \alpha\varphi)\mu]z^2 \\ + \{(1 + [2\varphi(1 - \varphi) + \alpha(1 - 2\varphi)]\mu\} z + (1 - \varphi)(1 - \varphi - \alpha)\mu, \end{aligned} \quad (2.85)$$

$$C_{ff}(z) = \{z^2 - [2 - \varsigma(1 + \beta)]z + 1 - \varsigma\beta\} \quad (2.86)$$

$$C_{fs}(z) = (\varphi + \alpha)(1 + \beta)z^2 + [(1 + \beta - (\varphi + \alpha)(1 + 2\beta))z - \beta(1 - \varphi - \alpha)], \quad (2.87)$$

$$C_{sf}(z) = (\varphi z + 1 - \varphi). \quad (2.88)$$

Observe that $C_{ff}(z)$ and $C_{ss}(z)$ with $\mu = 0$ are the characteristic polynomials for the uncoupled fluid-volume and structure, respectively, while $C_{fs}(z)$ and $C_{sf}(z)$ account for the cross-coupling. Plainly the stability region of $C(z)$ cannot extend beyond that of the uncoupled components. Since $C_{ss}(z)$ is absolutely stable (A -stable) with the choice $1/2 \leq \varphi \leq 1$, the stability region of (2.84) must lie inside that of $C_{ff}(z)$, which is in fact given by (2.50).

A long but straightforward analysis shows that the quintic polynomial $\check{C}(z)$ has a double root at $z = 1$. Removing the factor $(z - 1)^2$ reduces $\check{C}(z)$

to a *cubic* polynomial:

$$C(z) = z C_f(z) - \varsigma \mu C_m(z), \quad (2.89)$$

where ς is given by (2.46), and

$$C_f(z) = z^2 - [2 - \varsigma(1 + \beta)]z + 1 - \varsigma\beta, \quad (2.90)$$

$$\begin{aligned} C_m(z) &= \varphi(\varphi + \alpha)z^2 + 2\varphi(1 - \varphi) + \alpha(1 - 2\varphi)z + (1 - \varphi)(1 - \varphi - \alpha) \\ &= (\varphi z + 1 - \varphi)[(\varphi + \alpha)z + 1 - \varphi - \alpha], \end{aligned} \quad (2.91)$$

[Note that $C_f(z)$ is precisely (2.47).] The stability of $C(z)$ was studied with a computer program. Some results of the study are shown in Figures 2 through 5. In these figures the stability region is plotted in the h, β plane over the "window"

$$0 \leq h/h_C \leq 1, \quad 0 \leq \beta \leq 1, \quad (2.92)$$

where h_C is the critical (Courant) timestep (2.32) for an uncoupled and undamped ($\beta = 0$) fluid-volume mesh. The other three free parameters are φ , α and μ , which characterize the integration formula (2.70)-(2.71), the interaction term predictor (2.75), and the modal coupling strength, respectively. The parameter ς is implicitly defined by h/h_C , since $\varsigma = 4(h/h_C)^2$ from (2.49) for $\beta = 0$ and $\gamma = 1$.

Figure 2 show stability regions for the trapezoidal rule ($\varphi = 1/2$) when $\alpha = 0$, i.e. the last displacement solution is used in the interaction term b^s , as in (2.63). The eight frames shown in Figure 2 pertain to fixed values of

$$\mu_C = \frac{\rho \alpha^2 c^2 h_C^2}{mq}, \quad (2.93)$$

which is simply (2.82) evaluated at the Courant timestep. This is the critical *physical* parameter as regards stability of the staggered time-integration procedure. The values of μ_C for the eight frames are listed in the figure caption. Stable regions are dark shaded. The stable region for $\mu_C = 0$ corresponds to the no-interaction case, whose equation is (2.50). It can be seen that as μ_C increases, the fluid damping coefficient β can have a dramatic effect on stability. For example, if $\mu_C = 1$, the largest stable h is virtually zero if $\beta = 0$, but surges to about $0.81h_C$ if $\beta = 0.25$. This effect should be contrasted to the uncoupled case studied in §2.4, in which increasing β always reduces the stable stepsize. But even with damping help in the range $0 \leq \beta \leq 1$, no stable stepsize in the window (2.91) essentially survives for $\mu_C > 5$.

Figure 3 also pertains to the trapezoidal rule, but now α is 1, which effectively amounts to using the predictor (2.69). It can be seen that use of this predictor substantially extends the stability region for large μ_C . The effect of the damping coefficient β is not so dramatic as in the previous case, but it is still pronounced for high μ_C values.

"Overpredicting" with $\alpha > 1$ has even more beneficial effects on stability, as evidenced by Figure 4, which corresponds to $\alpha = 2$. But accuracy suffers, so using $\alpha = 1$ is recommended.

Finally, Figure 5 shows results for the Backward Euler method ($\varphi = 1$). This integrator introduces high numerical damping in the structure, whereas the trapezoidal rule introduces none. The stability regions for large μ_C are substantially enlarged, and are now fairly insensitive to both β and α (effect of the latter is not shown here.)

Mesh Sizing Guidelines. The fact that μ_C is the critical stability parameter for fluid-structure coupling may be used to derive some dimensioning guidelines for the fluid-volume mesh.

It is assumed that the wet-surface structure is a shell, the discretization of which is known *a priori*. Now consider the interaction between two adjacent physical elements: (1) a square plate dimensioned $L \times L$, with thickness t_s and density ρ_s , and (2) a rectangular fluid-volume brick dimensioned $L \times L \times D$, where $D \leq L$ is the dimension normal to the plate. The contact area is $L \times L$. Replacing

$$h_C^2 = D^2/c^2, \quad a^2 = L^4, \quad m = \rho_s L^2 t_s, \quad q = L^2 D/2, \quad (2.94)$$

into (2.93) yields

$$\mu_C = \frac{2\rho D}{\rho_s t_s} \quad (2.95)$$

For steel in water, $\rho_s/\rho \approx 8$, so that

$$\mu_C \approx \frac{D}{4 t_s} \quad (2.96)$$

This can be used for an order-of-magnitude (generally conservative) estimate of μ_C for high-frequency, *localized* "mesh modes". The estimate helps in sizing the first layer of fluid-volume elements adjacent to the structure. The mesh can then be "radially" continued into the fluid as far as necessary.

For example, suppose that $t_s = 2$ inches, and that it is desired to keep $\mu_C < 5$ from stability considerations. Then D should not exceed 40 inches.

This simple rule has been used to size the fluid-volume meshes for the example problems presented in Section IV, so that μ_C does not exceed 5.

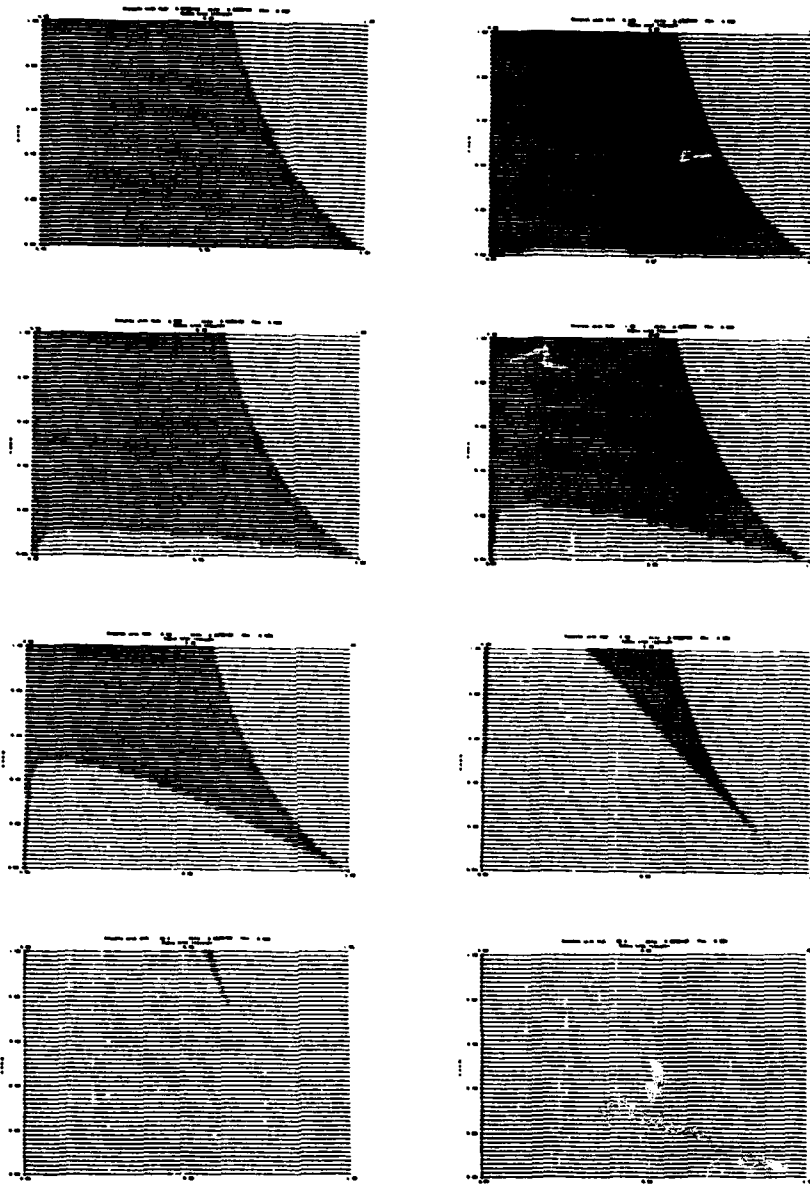


Figure 2. Stability of (2.84) for trapezoidal rule ($\varphi = 0.5$) and last-solution predictor $\alpha = 0$. Each frame covers the "window" $0 \leq h/h_C \leq 1$ horizontally and $0 \leq \beta \leq 1$ vertically. Stable regions are dark shaded. Starting from the upper left corner, the eight frames correspond to the following values of μ_C : 0, 0.1, 0.5, 1.0, 2.0, 5.0, 10.0 and 20.0.

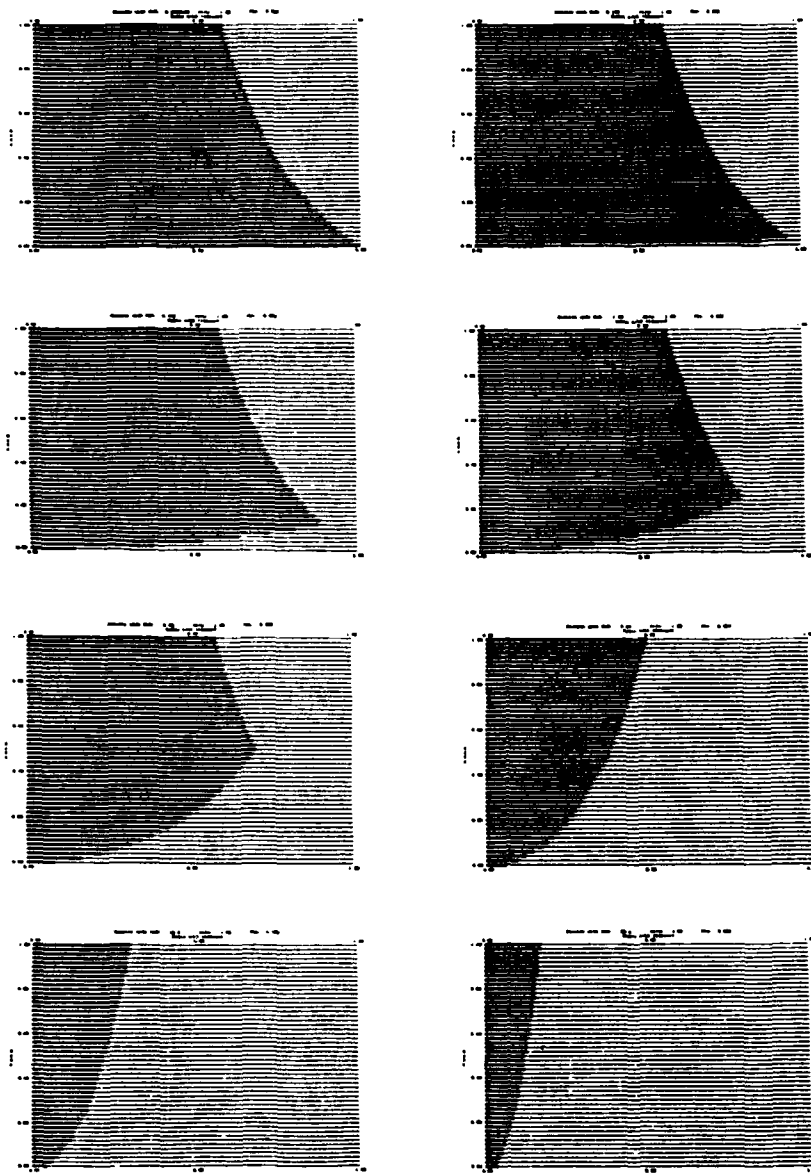


Figure 3. Stability of (2.84) for trapezoidal rule ($\varphi = 0.5$) and full-step predictor $\alpha = 1$. Each frame covers the "window" $0 \leq h/h_C \leq 1$ horizontally and $0 \leq \beta \leq 1$ vertically. Stable regions are dark shaded. Starting from the upper left corner, the eight frames correspond to the following values of μ_C : 0, 0.1, 0.5, 1.0, 2.0, 5.0, 10.0 and 20.0.

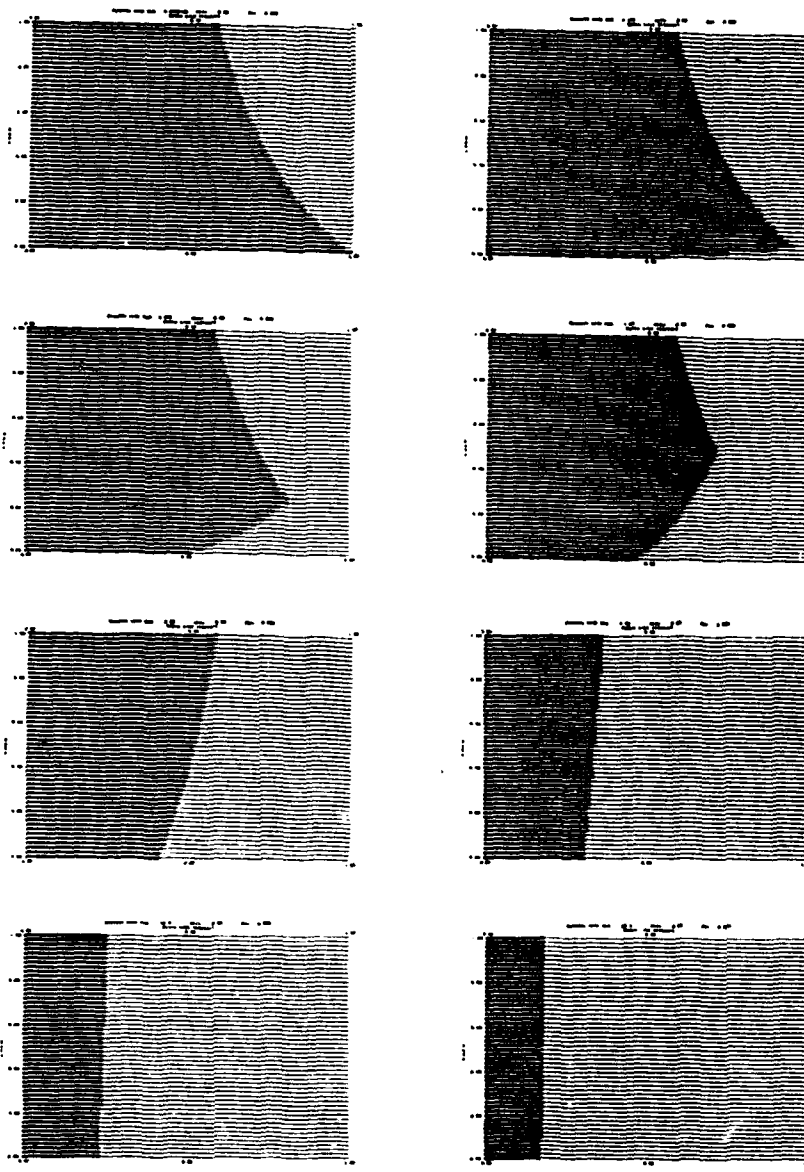


Figure 4. Stability of (2.84) for trapezoidal rule ($\varphi = 0.5$) and “overextrapolated” predictor $\alpha = 2$. Each frame covers the “window” $0 \leq h/h_C \leq 1$ horizontally and $0 \leq \beta \leq 1$ vertically. Stable regions are dark shaded. Starting from the upper left corner, the eight frames correspond to the following values of μ_C : 0, 0.1, 0.5, 1.0, 2.0, 5.0, 10.0 and 20.0.

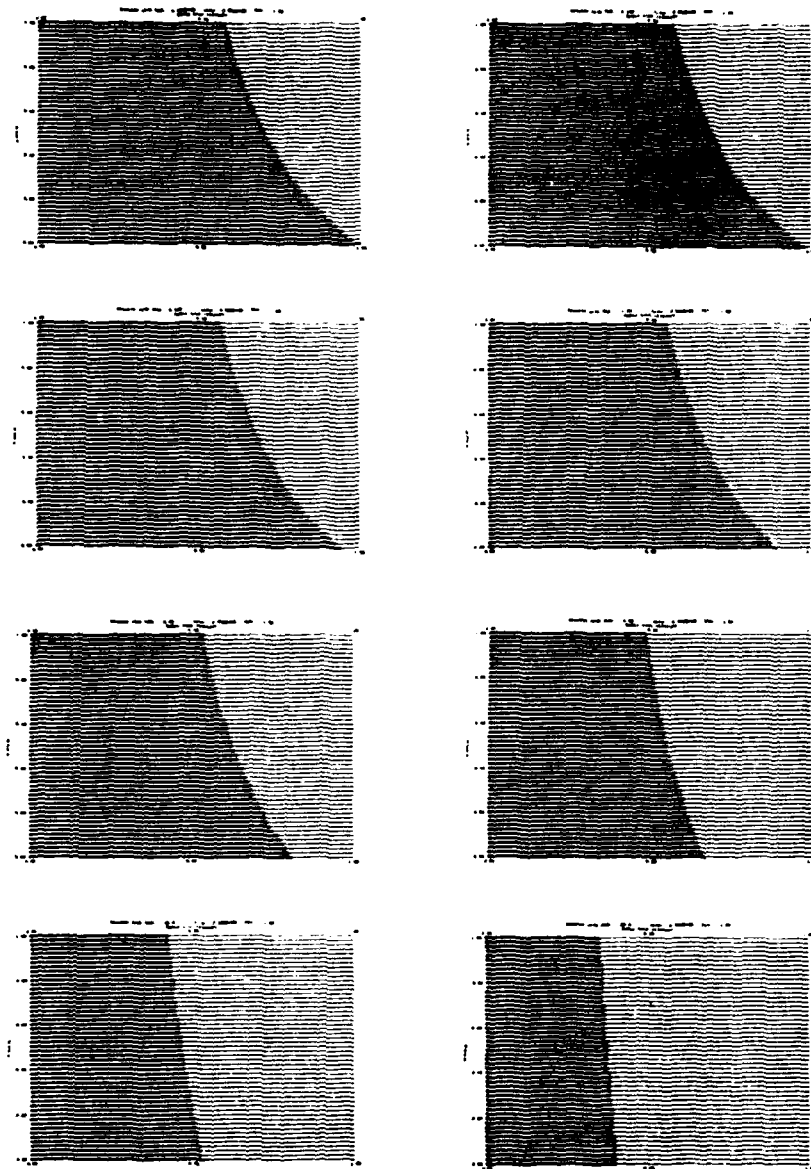


Figure 5. Stability of (2.84) for Backward Euler ($\varphi = 1$) and last-solution predictor $\alpha \approx 0$. Each frame covers the "window" $0 \leq h/h_C \leq 1$ horizontally and $0 \leq \mu \leq 1$ vertically. Stable regions are dark shaded. Starting from the upper left corner, the eight frames correspond to the following values of μ_C : 0, 0.1, 0.5, 1.0, 2.0, 5.0, 10.0 and 20.0.

§2.6 Fluid-DAA Interaction

Role of DAA Boundary. The Doubly Asymptotic Approximation (DAA) boundary truncates the fluid-volume mesh to finite extent. In its discrete form, it consists of boundary elements in contact with faces of fluid-volume brick elements. This computational field should ideally operate as a transparent entry boundary for incoming (incident) waves, and as a perfectly radiating boundary for outgoing waves. Because of the nature of the DAA, these conditions are asymptotically satisfied in the limit of high-frequency and low-frequency motions, and approximately otherwise.

The DAA boundary element mesh is usually constructed so that its nodes coincide with fluid-volume nodes. The net result is that DAA elements lie on brick faces. But all DAA computational vectors are expressed not in terms of nodal point values, but rather of values at *control points*, which are located at the centroid of each DAA element. So it sometimes becomes necessary to distinguish quantities such as displacement and pressure vectors, area matrices, etc., which can be referred to either set of points.

In this and following sections, letters *f* and *d* applied as subscripts or superscripts to a matrix or vector symbol are used to indicate that it pertains to DAA control points and to fluid-volume nodes located on the DAA boundary, respectively; for example, total-pressure vectors \mathbf{p}^f and \mathbf{p}^d . If neither appears, *d* is assumed.

Boundary Interaction Terms. The DAA boundary acts on the fluid volume through the forcing term \mathbf{b}^d of (2.24). Arguments similar to those used in §2.5 can be offered to derive a formal matrix expression that relates \mathbf{b}^d to the vector \mathbf{x}^f of global (X, Y, Z) displacements at the DAA control points:

$$\mathbf{b}^d = \rho \mathbf{A}_d \mathbf{G}_{df} \mathbf{\Upsilon}_f \mathbf{x}^f \quad (2.97)$$

Here \mathbf{A}_d is a diagonal matrix of contributing areas that surround fluid-volume nodes, \mathbf{G}_{df} is a transformation matrix from DAA

control points to fluid-volume nodes, and Υ_f is a diagonal matrix of direction cosines of the boundary normal (positive going into the fluid) evaluated at the DAA control points. As in the case of the structure interaction, entries of \mathbf{A}_d and \mathbf{G}_{df} need never be explicitly computed, for the whole vector transformation process is elegantly hidden by one-point Gauss isoparametric integration.

The DAA displacement vector \mathbf{x}^f may be decomposed into three components due to the free-field incident wave, scattered wave, and hydrostatic pressure:

$$\mathbf{x}^f = \mathbf{x}^{fI} + \mathbf{x}^{fS} + \mathbf{x}^{fH}. \quad (2.98)$$

The hydrostatic displacement (but *not* the pressure) may be set to zero *ab initio*, as it cancels out in the relative displacement formulation used here. The other two components are studied in the following subsections.

Incident Wave. We consider incident spherical and plane waves. An incident spherical waveform is completely defined by giving its origin (charge location) and the pressure profile

$$p^I(t - t_0; R) \quad (2.99)$$

recorded at a reference location whose distance to the wave origin is R . As the wave clock can be adjusted through an arbitrary time shift t_0 , the reference location may be conveniently specified as the fluid-volume node “touched” by the wavefront at the reference time $t = 0$; for this node $R = R_0$. The free-field incident pressure can then be readily calculated at any fluid point for all times $-R_0/c \leq t < +\infty$.

The free-field fluid-particle displacement \vec{x}^I at an arbitrary point joined to the wave origin through the unit direction vector \vec{R} may be determined from the relation

$$\vec{x}^I(t) = \left(\frac{1}{\rho c} \vec{p}^I + \frac{1}{\rho R} \vec{p}^{*I} \right) \vec{R}. \quad (2.100)$$

where each superscript asterisk denotes *temporal integration* from $t = -R_0/c$ through t . This formula can be specialized to DAA control points to provide the matrix expression

$$\mathbf{\Gamma}_f \mathbf{x}^{fI} = \frac{1}{\rho c} \mathbf{\Gamma}_f \mathbf{\hat{p}}^{fI} + \frac{1}{\rho} \mathbf{R}^{-1} \mathbf{\Gamma}_f \mathbf{\hat{p}}^{*fI}, \quad (2.101)$$

where \mathbf{R} is a diagonal matrix containing distances from the wave origin to DAA control points, and $\mathbf{\Gamma}_f$ is a diagonal matrix of the cosines of the angles between the local propagation direction \vec{R} and the outward unit normal vectors at the DAA control points.

For an incident plane-wave, $R \mapsto \infty$, and the second term on the right of (2.101) drops out.

Scattered Waves. Displacements caused by scattered waves are calculated from the simplest Doubly Asymptotic Approximation, which reads

$$\mathbf{M}_f \mathbf{\hat{p}}^{fS} + \rho c \mathbf{A}_f \mathbf{p}^{fS} = \rho c \mathbf{M}_f \mathbf{\hat{u}}^{fS}. \quad (2.102)$$

In this equation, \mathbf{p}^{fS} and \mathbf{u}^{fS} are column vectors of scattered-wave pressures and normal fluid-particle velocities, respectively, at DAA control points, \mathbf{M}_f is the (fully populated) mass matrix for irrotational incompressible motions of the fluid external to the DAA, and \mathbf{A}_f is a diagonal matrix of boundary element areas.

To get \mathbf{x}^{fS} , integrate (2.102) twice in time, and solve for the scattered normal displacements that appear on the right-hand side:

$$\mathbf{\Gamma}_f \mathbf{x}^{fS} = \frac{1}{\rho c} \mathbf{\hat{p}}^{fS} + \mathbf{M}_f^{-1} \mathbf{A}_f \mathbf{\hat{p}}^{*fS}, \quad (2.103)$$

where constants of integration for $\mathbf{\hat{p}}^{fS}$ and $\mathbf{\hat{p}}^{*fS}$ are determined from the initial conditions discussed in §2.7.

Remark. Do not confuse \mathbf{A}_f with the \mathbf{A}_d that appears in (2.97). Both are diagonal area matrices but the first one pertains to DAA control points and the second one to fluid-volume nodes at the DAA boundary.

Mass/Damping Split. The two components of \mathbf{x}^{fS} that appear in (2.103) have different physical significance and deserve to be identified separately:

$$\mathbf{x}^{fD} = \frac{1}{\rho c} \mathbf{T}_f^{-1} \mathbf{\hat{p}}^{fS}, \quad (2.104)$$

$$\mathbf{x}^{fM} = \mathbf{T}_f^{-1} \mathbf{M}_f^{-1} \mathbf{A}_f \mathbf{\hat{p}}^{**fS}. \quad (2.105)$$

Here superscripts D and M stand for damping and mass, respectively, in accordance with the following interpretation.

The displacement vector \mathbf{x}^{fD} corresponds to the DAA operating as a “ ρc boundary”, radiating high-frequency energy out into the external fluid. The displacement vector \mathbf{x}^{fM} corresponds to the DAA acting as an “added-mass boundary”, accounting rigorously for low-frequency “sloshing” of the external fluid. As discussed later, these different interpretations translate into different numerical treatments in the implementation of the time integration procedure.

Insertion of the various displacement terms into (2.97) — with the hydrostatic component excluded — splits the interaction vector into three components:

$$\mathbf{b}^d = \mathbf{b}^I + \mathbf{b}^D + \mathbf{b}^M \quad (2.106)$$

where

$$\mathbf{b}^I = \mathbf{A}_d \mathbf{G}_{df} \Gamma_f \left(\frac{1}{c} \mathbf{\hat{p}}^{fI} + \mathbf{R}^{-1} \mathbf{\hat{p}}^{*fI} \right), \quad (2.107)$$

$$\mathbf{b}^D = \frac{1}{c} \mathbf{A}_d \mathbf{G}_{df} \mathbf{\hat{p}}^{fS}, \quad (2.108)$$

$$\mathbf{b}^M = \rho \mathbf{A}_d \mathbf{G}_{df} \mathbf{M}_f^{-1} \mathbf{A}_f \mathbf{\hat{p}}^{**fS}. \quad (2.109)$$

Scattered Pressure Calculations. The fluid volume acts on DAA boundary elements through the total-pressure vector \mathbf{p} , which is obtained in the course of the time integration solution process. Total pressures may be interpolated from fluid-volume nodes to DAA control points through the transformation matrix $\mathbf{G}_{fd} = \mathbf{G}_{df}^t$:

$$\mathbf{p}^f = \mathbf{G}_{fd} \mathbf{p}^d. \quad (2.110)$$

The scattered pressure component now follows by subtracting off the incident and hydrostatic components:

$$\mathbf{p}^{fS} = \mathbf{p}^f - \mathbf{p}^{fI} - \mathbf{p}^{fH}. \quad (2.111)$$

This scattered pressure data can be time-integrated numerically to generate $\hat{\mathbf{p}}_n^{fS}$ and $\hat{\mathbf{p}}_{n+1}^{fS}$. For example, using the trapezoidal rule:

$$\hat{\mathbf{p}}_{n+1}^{fS} = \hat{\mathbf{p}}_n^{fS} + \frac{h}{2}(\mathbf{p}_n^{fS} + \mathbf{p}_{n+1}^{fS}), \quad (2.112)$$

$$\hat{\mathbf{p}}_{n+1}^{*fS} = \hat{\mathbf{p}}_n^{*fS} + \frac{h}{2}(\hat{\mathbf{p}}_n^{fS} + \hat{\mathbf{p}}_{n+1}^{fS}). \quad (2.113)$$

Finally, these pressure-integral values can be inserted into (2.108) and (2.109) to close the interaction loop.

Pressure Correction. Computational experiments with a fully staggered solution procedure for the DAA interaction have shown that undesirable pressure oscillations develop near the DAA boundary. These oscillations are caused by the time lag in the treatment of the “ ρc -boundary” coupling term (2.104). This lag interferes with the energy-radiation process for outgoing scattered waves. The spurious pressure oscillations eventually reflect back to the structure and distort its response.

The problem has been solved by using a *simultaneous pressure solution* for the ρc -boundary term, while the “added mass” term (2.105) is treated by staggered-solution techniques. The

whole business can be transacted at the node level. Thus, consider an individual fluid-volume node located at the DAA boundary. Rewrite the interaction term (2.108) as

$$b^D = (a_d/c) \hat{p}^S, \quad (2.114)$$

where b^D , a_d and \hat{p}^S denote entries of vectors \mathbf{b}^D , $\text{diag}(\mathbf{A}_d)$ and $\mathbf{G}_{df} \hat{\mathbf{p}}^S$, respectively, pertaining to the node under consideration. Next, time-discretize (2.114) through the trapezoidal rule (2.112):

$$b_{n+1}^D = (a_d/c) [\hat{p}_n^S + (h/2)(p_n^S + p_{n+1}^S)]. \quad (2.115)$$

Now use $p_{n+1}^S = p_{n+1} - p_{n+1}^I - p_{n+1}^H$ to get

$$b_{n+1}^D = (a_d/c) [\hat{p}_n^S + (h/2)(p_n^S - p_{n+1}^I - p_{n+1}^H + p_{n+1})]. \quad (2.116)$$

According to the problem-modelling assumptions stated in §2.1, cavitation should not occur at the DAA boundary. Hence the nodal pressure calculation, given by (2.67)-(2.68), becomes

$$\begin{aligned} \hat{q}(p_{n+1} - p^{II}) &= c^2(r + b_{n+1}^I + b_n^M) + \\ &c a_d [\hat{p}_n^S + \frac{h}{2}(p_n^S - p_{n+1}^I - p_{n+1}^H + p_{n+1})] \end{aligned} \quad (2.117)$$

where r , \hat{q} , b^I and b^M are entries of vectors $\mathbf{r} = -\mathbf{H}\Psi$, $\text{diag}(\tilde{\mathbf{Q}})$, \mathbf{b}^I and \mathbf{b}^M , respectively, for the node under consideration. The next total-pressure value p_{n+1} appears on both sides of this equation. For simultaneous solution, the unknown term is moved to the left, giving

$$\hat{q} p_{n+1} = \hat{q}(1 + \kappa)p_{n+1} = g, \quad (2.118)$$

where

$$\kappa = \frac{1}{2\hat{q}} c h a_d, \quad (2.119)$$

and g embodies all "leftover" right-hand side components. The net effect of all this is that *diagonal entries of $\tilde{\mathbf{Q}}$ pertaining to*

fluid-volume nodes on the DAA boundary must be multiplied by a correction factor $1 + \kappa$.

Remark 1. The correction factor $(1 + \kappa)$ is stepsize dependent, and tends to one as $h \mapsto 0$. It is fairly easy to show that $\kappa \leq 1$ if $h \leq h_C$, and takes the value 1 on a regular grid if h equals the Courant stepsize h_C .

Remark 2. $\kappa\bar{q}$ is half of the fluid volume swept by an area a_d over the distance ch travelled by a sound wave over the time increment h .

Remark 3. Since the pressure correction is node-level, the basic philosophy of the staggered solution procedure, which calls for only vector transfer information, is not violated. Had the simultaneous solution procedure been extended to include the fluid-mass interaction vector \mathbf{b}^M , the fluid volume analyzer would need to know about the full matrix \mathbf{M}_f .

Remark 4. In the terminology of coupled-system partitioned analysis, the process by which selected field quantities are manipulated into the left-hand side of the equations of another field is called *augmentation*. This technique is primarily used to improve numerical stability characteristics [8].

Staged DAA Analysis. Introduction of the pressure correction mechanism effectively splits the analysis of the DAA field into two stages. In the first stage, the DAA displacement vector

$$\mathbf{x}^f = \mathbf{x}_{n+1}^{fI} + \mathbf{x}_n^{fD} + \mathbf{x}_{n+1}^{fMP} \quad (2.120)$$

is evaluated and supplied to the fluid volume analyzer. In (2.120), \mathbf{x}_{n+1}^{fMP} is a *predictor* for \mathbf{x}_{n+1}^{fM} . This term is generated by extrapolating the double integral of scattered pressure, for example

$$\mathbf{\hat{p}}_{n+1}^{fSP} = \mathbf{\hat{p}}_n^{fS} + h \mathbf{\hat{p}}_n^{fS}, \quad (2.121)$$

which is then inserted in (2.109). The primary advantage of predicting \mathbf{b}_{n+1}^{fM} , rather than using the previous value, is to improve numerical stability characteristics, as shown later in this section.

The second stage begins on exit from the fluid-volume analyzer, which returns the total pressure vector \mathbf{p}_{n+1}^d . Now the scattered pressure-integral terms can be *corrected* using Equations (2.110) to (2.113).

For the *implementation* of this staged process it is more convenient to use an incremental formulation based upon the total pressure rather than the scattered pressure, as described next.

Incremental Formulation. Although the value of \mathbf{x}^f accumulated since $t = 0$ given in (2.120) must be supplied to the fluid-volume analyzer, in practice it is convenient to handle the DAA computations *incrementally*, since some terms are known precisely while others must be estimated and then subsequently corrected.

The known terms involve the incident and hydrostatic pressure. Some of them arise because of the DAA formulation, which is based on the scattered pressure, and the need to work with total pressure for the implicit treatment of the ρc boundary term. They are:

$$\Delta \hat{\mathbf{p}}^{fI} = \hat{\mathbf{p}}_{n+1}^{fI} - \hat{\mathbf{p}}_n^{fI}, \quad (2.122)$$

$$\Delta \hat{\mathbf{p}}^{*fI} = (h/2)(\hat{\mathbf{p}}_{n+1}^{fI} + \hat{\mathbf{p}}_n^{fI}), \quad (2.123)$$

$$\Delta \hat{\mathbf{p}}^{fH} = h \mathbf{p}^H, \quad (2.124)$$

$$\hat{\mathbf{p}}_{n+1}^{fH} = \hat{\mathbf{p}}_n^{fH} + \Delta \hat{\mathbf{p}}^{fH}, \quad (2.125)$$

$$\Delta \hat{\mathbf{p}}^{*fH} = h(1 + \frac{h}{2t}) \hat{\mathbf{p}}_{n+1}^{fH}. \quad (2.126)$$

Hence

$$\begin{aligned} \Upsilon_f \Delta \mathbf{x}_{k \text{ now } n}^f &= -\frac{1}{\rho c}(\Delta \hat{\mathbf{p}}^{fI} + \Delta \hat{\mathbf{p}}^{fH}) - \mathbf{M}_f^{-1} \mathbf{A}_f (\Delta \hat{\mathbf{p}}^{*fI} + \Delta \hat{\mathbf{p}}^{*fH}) \\ &\quad + \frac{1}{\rho c} \Gamma_f \Delta \hat{\mathbf{p}}^{fI} + \frac{1}{\rho} \Gamma_f \mathbf{R}^{-1} \Delta \hat{\mathbf{p}}^{*fI}. \end{aligned} \quad (2.127)$$

The unknown terms that must be estimated involve integrals of the total pressure as

$$\Delta \hat{\mathbf{p}}^f = h \mathbf{p}_n^f, \quad (2.128)$$

$$\Delta \hat{\mathbf{p}}^{*f} = h \hat{\mathbf{p}}_n^f, \quad (2.129)$$

$$\Upsilon_f \Delta \mathbf{x}_{estimated}^f = \frac{1}{\rho c} \Delta \dot{\mathbf{p}}^f + \mathbf{M}_f^{-1} \mathbf{A}_f \Delta \ddot{\mathbf{p}}^{*f}. \quad (2.130)$$

The predicted value of \mathbf{x}_{n+1}^f that is supplied to the fluid-volume analyzer is then

$$\mathbf{x}_n^{fP} = \mathbf{x}_n^f + \Delta \mathbf{x}_{known}^f + \Delta \mathbf{x}_{estimated}^f. \quad (2.131)$$

On return from the fluid-volume analysis, displacements and pressures are corrected:

$$\Delta \dot{\mathbf{p}}^f = (h/2)(\mathbf{p}_{n+1}^f + \mathbf{p}_n^f), \quad (2.132)$$

$$\dot{\mathbf{p}}_{n+1}^f = \dot{\mathbf{p}}_n^f + \Delta \dot{\mathbf{p}}^f, \quad (2.133)$$

$$\Delta \ddot{\mathbf{p}}^{*f} = (h/2)(\ddot{\mathbf{p}}_{n+1}^f + \ddot{\mathbf{p}}_n^f), \quad (2.134)$$

$$\Upsilon_f \Delta \mathbf{x}_{corrected}^f = \frac{1}{\rho c} \Delta \dot{\mathbf{p}}^f + \mathbf{M}_f^{-1} \mathbf{A}_f \Delta \ddot{\mathbf{p}}^{*f}, \quad (2.135)$$

$$\mathbf{x}_{n+1}^j = \mathbf{x}_n^j + \Delta \mathbf{x}_{known}^j + \Delta \mathbf{x}_{corrected}^j. \quad (2.136)$$

Notice that in this formulation there is no need to keep track of the accumulated double integral of pressure $\ddot{\mathbf{p}}^{*f}$.

Stability of Staggered Integration. The following stability analysis only investigates the effect of staggering the fluid-mass coupling term \mathbf{b}^M . The radiation-damping term \mathbf{b}^D has no effect on stability, for it is treated implicitly. Incident and hydrostatic components are dropped and scattered pressure becomes pressure. Cavitation is ignored. Absolute, rather than incremental, quantities are used. Under these assumptions, the modal equations for the advancing step read:

$$\dot{\psi}_{n+1/2} = \dot{\psi}_{n-1/2} + h[(1+\beta)p_n - \beta p_{n-1}], \quad (2.137)$$

$$\psi_{n+1} = \psi_n + h \dot{\psi}_{n+1/2}, \quad (2.138)$$

$$\ddot{p}_{n+1}^{*P} = \ddot{p}_n^* + \alpha h \dot{p}_n, \quad (2.139)$$

$$b_n^M = \rho a_d \epsilon \ddot{p}_{n+1}^{*P}, \quad (2.140)$$

$$s_{n+1} = -\lambda \psi_{n+1} + b_n^M/q, \quad (2.141)$$

$$p_{n+1} = c^2 s_{n+1}, \quad (2.142)$$

$$\dot{p}_{n+1} = \dot{p}_n + (h/2)(p_n + p_{n+1}), \quad (2.143)$$

$$\ddot{p}_{n+1}^* = \dot{p}_n^* + (h/2)(\dot{p}_n + \dot{p}_{n+1}). \quad (2.144)$$

In these equations, ψ , s and p are *amplitudes* of Ψ , s and p , respectively, for a fluid-volume normal motion of eigenvalue λ , as in §2.5; a_d and q are generalized values of \mathbf{A}_d and $\tilde{\mathbf{Q}}$, respectively, the latter embodying appropriate pressure correction factors (2.119); α is a pressure-integral predictor coefficient; and ξ are the roots of the "fluid boundary mode" symmetric eigenproblem

$$\xi \mathbf{M}_f \mathbf{w} = \mathbf{A}_f \mathbf{w}, \quad (2.145)$$

\mathbf{w} being the boundary mode excited by the modal volume pressure.

Elimination of the intermediate variables $\dot{\psi}$ and s yields two coupled difference equations:

$$\psi_{n+1} - 2\psi_n + \psi_{n-1} = -h^2[(1+\beta)p_n - \beta p_{n-1}], \quad (2.146)$$

$$p_{n+1} - 4\nu h^{-2}(\dot{p}_n^* + \alpha h \dot{p}_n) = -\lambda c^2 \psi_{n+1}, \quad (2.147)$$

in which

$$\nu = \frac{\rho c^2 a_d \xi h^2}{4q}, \quad (2.148)$$

is a dimensionless modal-coupling coefficient that plays a rôle analogous to that of μ in §2.5. (The factor 4 is introduced for convenience in subsequent manipulations.) Transform these difference equations to the z plane, and eliminate the pressure-integral terms through the operator relations

$$\ddot{p}_n^* = \frac{h}{2} \frac{z+1}{z-1} \dot{p}_n = \frac{h^2}{4} \left(\frac{z+1}{z-1} \right)^2 p_n. \quad (2.149)$$

The resulting *cubic* characteristic polynomial is

$$C(z) = z C_f(z) - \varsigma \nu_C C_m(z), \quad (2.150)$$

where ς is given by (2.46).

$$C_f(z) = z^2 - [2 - \varsigma(1+\beta)]z + 1 - \varsigma\beta, \quad (2.151)$$

$$C_m(z) = (z+1)^2 + 2\alpha(z^2 - 1), \quad (2.152)$$

and ν_C is ν evaluated at the Courant timestep:

$$\nu_C = \frac{\rho c^2 a_d \xi h_C^2}{4q}, \quad (2.153)$$

The similarity of these expressions with (2.89) through (2.91) is apparent. Polynomial $C_f(z)$ is the same as (2.90), and $C_m(z)$ is precisely (2.91) if $\varphi = 1/2$. Thus the stability regions of (2.89) for the trapezoidal rule and of (2.151) coincide if μ_C and ν_C are identified. One can therefore refer to Figures 2 through 4 for the stability of $C(z)$ with varying α , simply by replacing μ^C by ν^C .

Estimating ν_C . To apply the conclusions of the stability analysis, it remains to obtain a ballpark upper-bound estimate for ν_C . To get it, an admittedly idealized situation is considered. Imagine that the DAA boundary is a sphere of radius R , and that adjacent fluid-volume elements are (roughly) bricks dimensioned $L \times L \times L$. Assume further that the fluid motions are axisymmetric fluid-boundary modes of a sphere (Legendre functions) with circumferential wave number m . The corresponding eigenroot ξ is then given by

$$\xi = \frac{a_f}{m_f} = \frac{\frac{4\pi R^2}{2m+1}}{\frac{4\pi \rho R^3}{(m+1)(2m+1)}} = \frac{m+1}{\rho R}. \quad (2.154)$$

Next, insert $a_d = L^2$, $q = L^3/2(1+\kappa)$, $h_C = L/c$, and (2.154) into (2.153) to get

$$\nu_C = \frac{(1+\kappa)(m+1)L}{2R}. \quad (2.155)$$

As the *coup de grace*, claim that the boundary mode wavelength is of the order of the fluid-volume mesh size L , so that

$$L \approx \frac{2\pi R}{m+1}. \quad (2.156)$$

this being clearly a worst-case scenario. Inserting (2.156) in (2.155) yields $\nu_C \approx \pi/(1+\kappa)$. Since $0 \leq \kappa \leq 1$,

$$\nu_C < \pi \approx 3, \quad (2.157)$$

which is the estimate sought.

§2.7 Response Calculation Details

This section meshes together the theoretical developments outlined in §2.3 through §2.6 with a starting procedure to put together a practical response calculation scheme.

The Reference State. Starting a staggered solution procedure that involves three computational fields and combines explicit and implicit integration methods is a delicate task. If the integration does not start right, it cannot be corrected. Furthermore, the starting procedure should be independent of whether the structure is linear or nonlinear, and be readily extendible to internal fluid problems, in which the motion of the structure boundary provides the input excitation.

To meet these goals, *the state at $t = 0$ is used as reference state*. Successive integration steps determine the deviation from the reference state, rather than the total state. For example, the total pressure vector at fluid volume nodes is actually broken down into *four* components:

$$\mathbf{p} = \mathbf{p}^H + \mathbf{p}_0^I + (\mathbf{p}^I - \mathbf{p}_0^I) + \mathbf{p}^S \quad (2.158)$$

and similarly for Ψ , $\dot{\Psi}$, \mathbf{s} , etc. The pressure determined by the central difference scheme is the reference state deviator

$$\mathbf{p}^I - \mathbf{p}_0^I + \mathbf{p}^S, \quad (2.159)$$

which added to the reference pressure

$$\mathbf{p}_0 = \mathbf{p}^H + \mathbf{p}_0^I \quad (2.160)$$

furnishes the total pressure \mathbf{p} . Extending this idea to the full coupled system leads to the following solution procedure.

Initialization. To start up the time integration process, do the following.

- **Hydrostatic Pressure.** Calculate hydrostatic pressure \mathbf{p}^H at all fluid volume nodes, structure wet-surface nodes, and DAA control points.
- **Incident Pressure.** Given a spherical or plane wave pressure profile, origin, and fluid volume node touched by the wavefront at $t = 0$ (the "wavefront node"), calculate the initial incident pressure \mathbf{p}_0^I at fluid volume nodes and DAA control points (The wavefront node may be in contact with the structure, but the front must not *intersect* the structure.)
- **Reference Structure Solution.** Calculate the static response of the structure to the hydrostatic pressure; let \mathbf{x}_0^S be the corresponding displacement vector. Initialize historic vectors.
- **Reference DAA Solution.** Calculate fluid-particle displacements at DAA control points due to hydrostatic pressure and initial incident wave. Initialize pressure integral vectors.
- **Stepsize.** Select initial time increment h .
- **Initial Velocity Potential.** Calculate $\Psi_{-1/2}$ at fluid volume nodes by integrating the incident wave flux from $t = -\infty$ to $t = -h/2$. (This may be done analytically for simple waveforms, and numerically otherwise.)
- **Initial Displacement Potential.** Calculate Ψ_0 at fluid volume nodes by doubly integrating the incident wave flux from $t = -\infty$ to $t = 0$. (Same remark as for the velocity potential calculation.)

Time Integration Process. For $n = 0, 1, \dots$, do the following.

- **Structure Analysis.** Solve the structure equations for the next displacement vector. In the case of a linear structure,

$$\mathbf{E}_s(\mathbf{x}_n^s - \mathbf{x}_0^s) = \mathbf{h}_n^s - \delta^2 \mathbf{G}_s \mathbf{A}_s \mathbf{p}_n. \quad (2.161)$$

- **DAA Boundary Analysis (1st Stage).** The incremental formulation described in §2.6 is used. At DAA control points, compute

$$\mathbf{p}_n^f = \mathbf{G}_{fd} \mathbf{p}_n^d, \quad (2.162)$$

$$\Delta \mathbf{\hat{p}}^{fI} = \mathbf{\hat{p}}_{n+1}^{fI} - \mathbf{\hat{p}}_n^{fI}, \quad (2.163)$$

$$\Delta \mathbf{\hat{p}}^{*fI} = (h/2)(\mathbf{\hat{p}}_{n+1}^{fI} + \mathbf{\hat{p}}_n^{fI}), \quad (2.164)$$

$$\Delta \hat{\mathbf{p}}^{fH} = h \mathbf{p}^H, \quad (2.165)$$

$$\hat{\mathbf{p}}_{n+1}^{fH} = \hat{\mathbf{p}}_n^{fH} + \Delta \hat{\mathbf{p}}^{fH}, \quad (2.166)$$

$$\Delta \hat{\mathbf{p}}^{*fH} = h(1 + \frac{h}{2t}) \hat{\mathbf{p}}_{n+1}^{fH}. \quad (2.167)$$

$$\begin{aligned} \Upsilon_f \Delta \mathbf{x}_{k \text{ known}}^f &= -\frac{1}{\rho c} (\Delta \hat{\mathbf{p}}^{fI} + \Delta \hat{\mathbf{p}}^{fH}) - \mathbf{M}_f^{-1} \mathbf{A}_f (\Delta \hat{\mathbf{p}}^{*fI} + \Delta \hat{\mathbf{p}}^{*fH}) \\ &\quad + \frac{1}{\rho c} \Gamma_f \Delta \hat{\mathbf{p}}^{fI} + \frac{1}{\rho} \Gamma_f \mathbf{R}^{-1} \Delta \hat{\mathbf{p}}^{*fI}. \end{aligned} \quad (2.168)$$

$$\Upsilon_f \Delta \mathbf{x}_{\text{estimated}}^f = \frac{h}{\rho c} \mathbf{p}_n^f + h \mathbf{M}_f^{-1} \mathbf{A}_f \hat{\mathbf{p}}_n^f. \quad (2.169)$$

$$\mathbf{x}_n^{fP} = \mathbf{x}_n^f + \Delta \mathbf{x}_{k \text{ known}}^f + \Delta \mathbf{x}_{\text{estimated}}^f. \quad (2.170)$$

• **Fluid Volume Analysis.** At fluid volume nodes, compute

$$\mathbf{s}_n = (\mathbf{s}_n - \mathbf{s}_{n-1})/h, \quad (2.171)$$

$$\dot{\Psi}_{n+1/2} = \dot{\Psi}_{n-1/2} + h(\mathbf{p}_n - \mathbf{p}^H + \beta h c^2 \mathbf{s}_n). \quad (2.172)$$

$$\dot{\Psi}_{n+1} = \Psi_n + h \dot{\Psi}_{n+1/2}. \quad (2.173)$$

$$\mathbf{r}_{n+1} = -\mathbf{H}(\Psi_{n+1} - \Psi_0), \quad (2.174)$$

$$\mathbf{b}_n^s = \rho \mathbf{A}_s \mathbf{G}_s (\mathbf{x}_n^s - \mathbf{x}_0^s), \quad (2.175)$$

$$\mathbf{b}_n^d = \rho \mathbf{A}_d \mathbf{G}_d \Upsilon_f (\mathbf{x}_n^{fP} - \mathbf{x}_0^f), \quad (2.176)$$

(where in (2.171) \mathbf{s}_{n-1} vanishes if $n = 0$). The pressure calculation steps depend on nodal boundary conditions, and are best stated in terms of node quantities. For internal fluid nodes,

$$s_{n+1} = r_{n+1}/\bar{q}, \quad (2.177)$$

$$p_{n+1} = \max(p^H + p_0^I + c^2 s_{n+1}, 0). \quad (2.178)$$

For nodes in contact with the structure,

$$s_{n+1} = (r_{n+1} + b_n^s)/\bar{q} \quad (2.179)$$

$$p_{n+1} = \max(p^H + p_0^I + c^2 s_{n+1}, 0). \quad (2.180)$$

For nodes in contact with the DAA boundary,

$$\kappa = ch a_d / (2\bar{q}), \quad (2.181)$$

$$s_{n+1} = s_n + \frac{(r_{n+1} + b_n^d) / \bar{q} - s_n}{(1 + \kappa)}, \quad (2.182)$$

$$p_{n+1} = p^H + c^2 s_{n+1}. \quad (2.183)$$

For nodes at a boundary of specified pressure \bar{p} (e.g. a free surface),

$$s_{n+1} = 0, \quad (2.184)$$

$$p_{n+1} = \bar{p}. \quad (2.185)$$

- **DAA Boundary Analysis (2nd Stage).** Return to the DAA analyzer to correct control point values:

$$\mathbf{p}_{n+1}^f = \mathbf{G}_{fd} \mathbf{p}_{n+1}^d. \quad (2.186)$$

$$\Delta \hat{\mathbf{p}}^f = (h/2)(\mathbf{p}_{n+1}^f + \mathbf{p}_n^f), \quad (2.187)$$

$$\hat{\mathbf{p}}_{n+1}^f = \hat{\mathbf{p}}_n^f + \Delta \hat{\mathbf{p}}^f, \quad (2.188)$$

$$\Delta \hat{\mathbf{p}}^{**f} = (h/2)(\hat{\mathbf{p}}_{n+1}^f + \hat{\mathbf{p}}_n^f), \quad (2.189)$$

$$\mathbf{T}_f \Delta \mathbf{x}_{corrected}^f = \frac{1}{\rho c} \Delta \hat{\mathbf{p}}^f + \mathbf{M}_f^{-1} \mathbf{A}_f \Delta \hat{\mathbf{p}}^{**f}, \quad (2.190)$$

$$\mathbf{x}_{n+1}^f = \mathbf{x}_n^f + \Delta \mathbf{x}_{known}^f + \Delta \mathbf{x}_{corrected}^f. \quad (2.191)$$

- **Advance.** Increment counter n by one, time t by h , and return to the structure subsystem. 

Section III

IMPLEMENTATION AND USAGE

§3.1 Implementation Overview

A number of modifications have been made to the standard USA-STAGS code in order to accomodate the CFA. In addition, one important assumption has been made that is implicit in the treatment of Section II and it should be clearly stated here. At this time the computational model does not allow the DAA boundary to be coincident with the structure boundary at any point. In other words, there must always be at least one layer of fluid volume elements between the structure and the DAA boundary, even if the problem under investigation involves internal fluid with non-cavitating external fluid. Relaxation of this restriction will be the subject of a future study into alternate forms of the interaction equations.

The stability analyses and starting procedure described in Section II clearly provide the groundwork for implementation of the USA-STAGS-CFA system; however, some additional comments are required as well as a reiteration of the interconnection between USA, STAGS, and the CFA. With regard to the starting procedure outlined in §2.7, it should be noted that a discontinuous wavefront cannot be propagated "as is" through the fluid volume mesh. Rather, the wavefront must be "ramped" so that its value at the front is one-half of the jump, in line with the Fourier convergence theorem. Only with this modification will a discontinuous wave propagate correctly.

Control of the transient analysis is governed by USA with STAGS and the CFA functioning as subroutines in the staggered solution strategy:

- Convert current pressures on structure boundary to forces and obtain structural solution with STAGS. Extrapolate displacements to $t + \Delta t$. If the structural behavior is linear the trapezoidal rule is used in STAGS and the extrapolation is that of (2.69). If the structural behavior is nonlinear the Park method is used in STAGS and the extrapolated value is taken to be the last value.
- Determine displacements on DAA boundary due to incident and hydrostatic pressure terms at $t + \Delta t$, transform current pressures on DAA boundary to control point values and estimate incremental displacements due to total pressure at $t + \Delta t$ from (2.169). Sum total estimated displacements on DAA boundary.
- Using as input the estimated displacements on the structure and DAA boundaries, solve for the fluid-volume pressures at $t + \Delta t$ using the CFA.
- Correct the DAA boundary displacements using the new total pressures.
- Save system responses and repeat cycle.

§3.2 Usage

Although the primary emphasis of this work has been on the development of the CFA and its interaction with USA-STAGS during a transient response analysis, a number of changes have been required in the processing that must precede the time integration phase of the computations. The following is a brief discussion of all of the steps involved.

- *STAGS Preprocessing.* Construct the structural model and create grid geometry file. Although the DAA equations used with the CFA are not augmented and the structural mass is no longer required for USA preprocessing the structural mass file is still generated because it also contains the node-point/degree-of-freedom information necessary for USA to apply pressure forces to the structure at their proper locations.
- *CFA Preprocessing.* Construct a file containing the following fluid volume information: node point coordinates, node connections to structure and DAA boundaries, node constraint tags, and, an element node list. It is important to note that the surface grid on the structure and the fluid volume grid in contact with the structure should be identical although the node numbering schemes need not be the same. In addition, the thickness of the volume elements in contact with the structure must be carefully sized to meet the stability criteria developed in §2.5.
- *USA Preprocessing.* The FLUMAS processor must access both the structure geometry file as well as the fluid volume file. Although fluid control points must be defined for USA on the DAA boundary and the added-mass matrix created, USA must keep track of the fluid-volume/structure connectivity. Even though augmentation is not carried out, the AUGMAT processor must be executed as it still functions to produce a compact data base file for USA to access during the transient response analysis.

- **USA-STAGS-CFA Processing.** The user must specify a level of artificial damping for the CFA and a "wavefront" node, i.e., the fluid volume node touched by the wavefront at $t = 0$, which will be generally be located as close as possible to the structure without actually being on it. Although the incident wave could be propagated all the way from the DAA boundary such practice is not recommended as computer time is simply wasted in producing mesh dispersion that erodes the wavefront sharpness. It is also important that the values chosen for the artificial damping and time stepsize meet the stability criteria stated in §§2.5-2.6.
- **USA Postprocessing.** Fluid pressure histories can be obtained at any fluid volume node desired as well as contour plots of the pressure field at specified times. A consequence of this capability is an increase in the size of the response history file for the USA-STAGS-CFA system over that for the USA-STAGS code.

Section IV

EXAMPLE PROBLEMS

§4.1 Overview

The USA-STAGS-CFA system has been tested by its application to two problems whose solutions have been obtained by other methods. The first is a one-dimensional problem studied by Bleich and Sandler [5], which involves a flat plate initially resting on the surface of a half space of fluid. The second is a two-dimensional cylindrical shell surrounded by an infinite fluid and is a variant of a problem discussed by Newton [6]. For both problems the excitation consists of a step-exponential plane wave superimposed upon an ambient hydrostatic pressure field.

§4.2 Bleich-Sandler Plate Problem

This is effectively a one-dimensional problem whose exact solution can be obtained by the method of characteristics. The USA-STAGS-CFA model consisted of

- (1) A single structural square plate of side dimension 1.5 in. and unit thickness.
- (2) 100 cubical fluid-volume elements of side dimension 1.5 in.
- (3) A DAA boundary with a single control point at the center of a square boundary element lying on a face of the last volume element.

Physical properties used were equivalent to those of [5]; however, they were converted to a computationally consistent set of units. The mass density of the plate was 5.32986×10^{-4} lb sec² in⁻⁴ while that of the fluid was 9.3455×10^{-5} lb sec² in⁻⁴. The speed of sound in the fluid was 57120 in sec⁻¹.

The hydrostatic pressure in the fluid at the plate mass was 14.7 psi, increasing linearly into the fluid volume consistent with a gravitational acceleration of $386.4 \text{ in sec}^{-2}$. The peak pressure of the incident wave was 103 psi and its decay time was $.9958 \times 10^{-4} \text{ sec}$.

The time step chosen for the analysis was $1.313 \times 10^{-5} \text{ sec}$ (one half of the Courant limit), which was kept constant for 1200 steps. Four sets of runs were made with and without cavitation allowed and using artificial damping coefficient values of $\beta = 0.0$, 0.25 , 0.50 and 1.00 . According to the stability analysis of §2.5 the integration process should be unstable for $\beta = 0.0$ but stable for the other three values and this was in fact verified.

Comparative results for the non-dimensional upward velocity of the plate are shown for the stable runs in Figures 6, 7, and 8. Actual velocities in in/sec can be obtained by multiplying by 57.12, while the time scale is given in decay time units. The solid lines are the USA-STAGS-CFA results whereas the discrete symbols are taken from the solution plots in [5]. The rapidly decaying curves that are essentially zero by 6 decay times are for the case when cavitation is not allowed while those that continue out to 12 and beyond illustrate the cutoff effects of cavitation.

As can be seen the correlation is excellent. The results show that the smoothing effects of the artificial damping have only slight influence on the amplitude and timing of the response. The small oscillations perceptible in Figure 6 are due to "ringing" and dispersive effects of the fluid-volume mesh, and gradually disappear as β is increased.

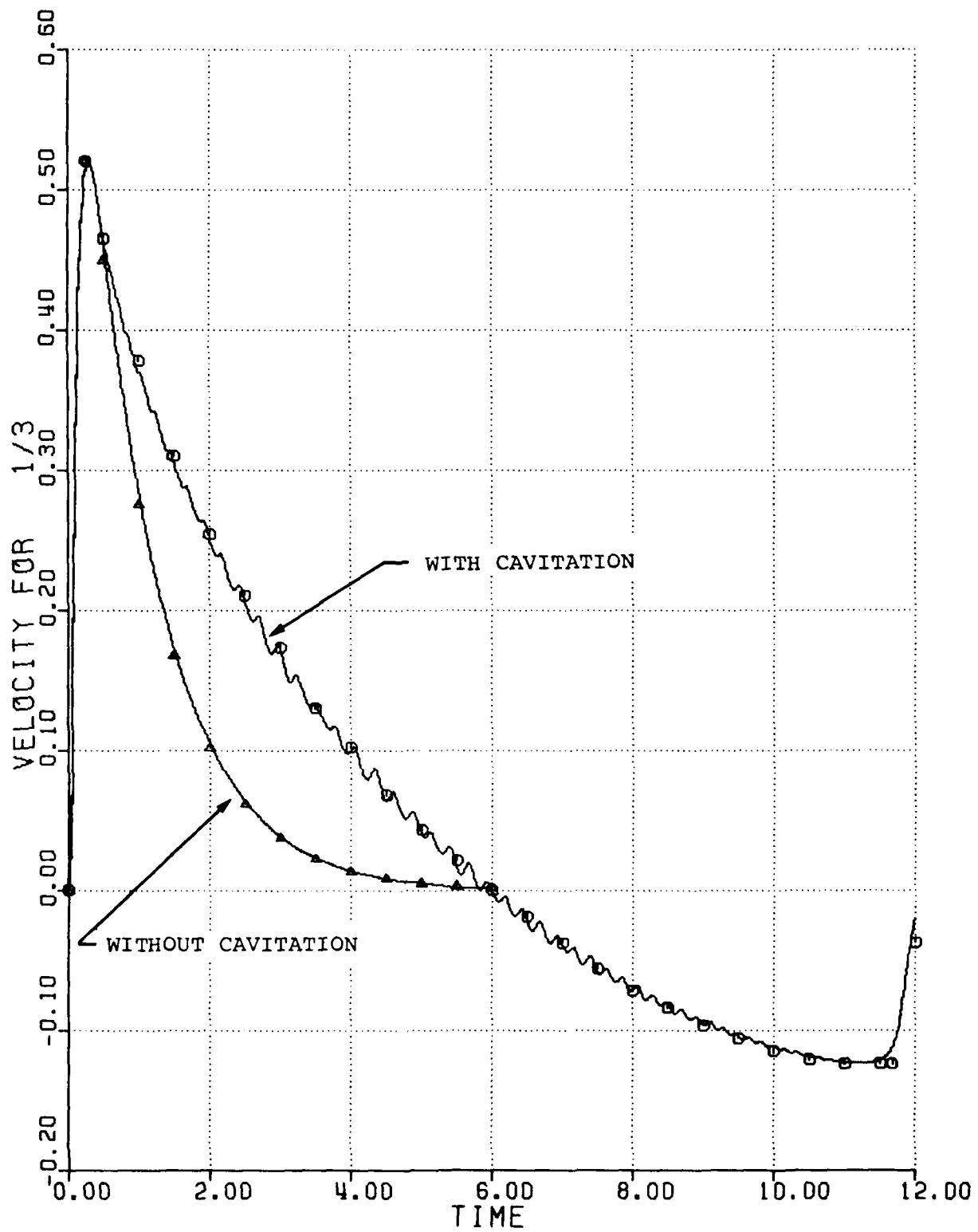


Figure 6 Non-dimensional upward velocity of plate, $\beta = 0.25$.

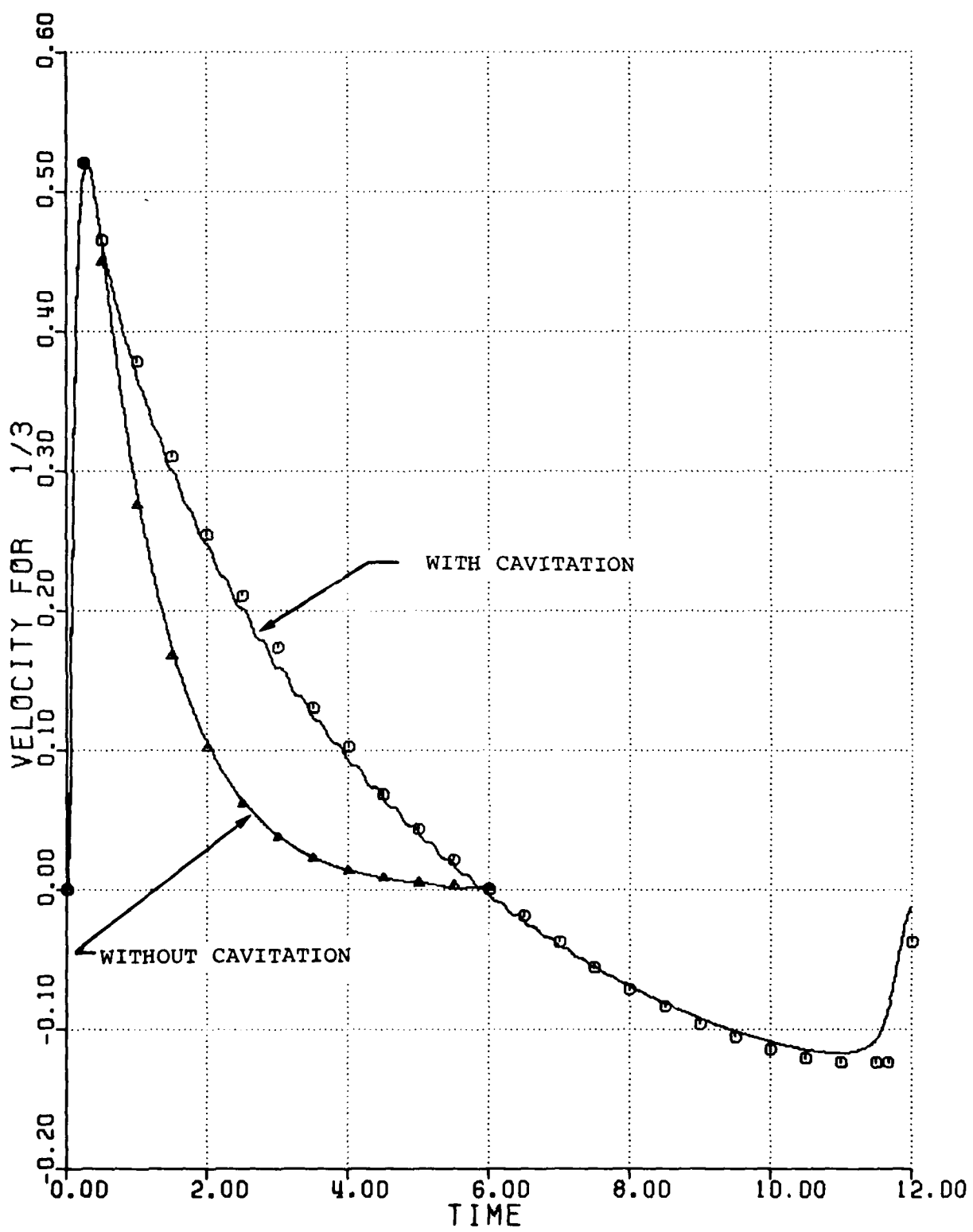


Figure 7 Non-dimensional upward velocity of plate, $\beta = 0.50$.

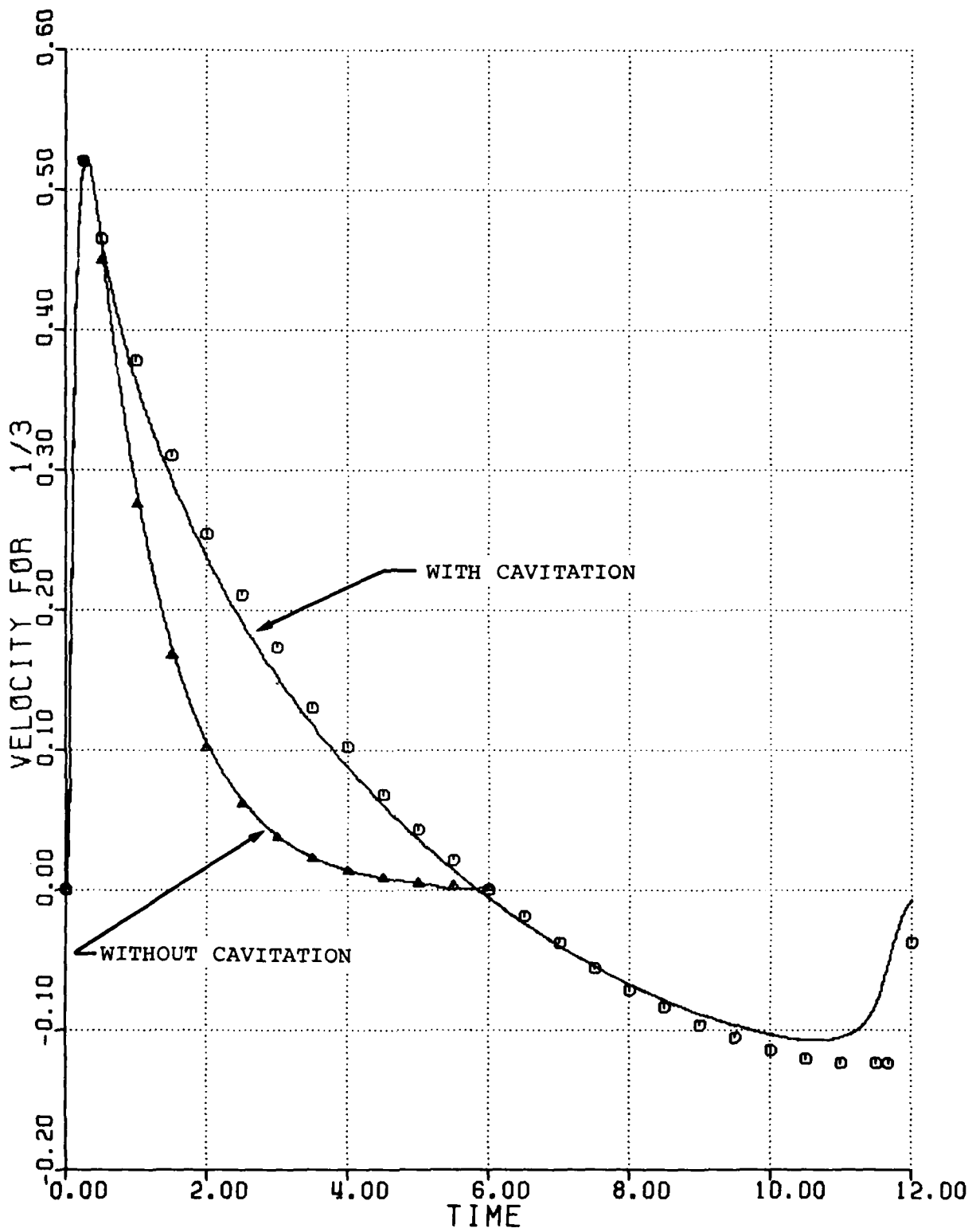


Figure 8 Non-dimensional upward velocity of plate, $\beta = 1.00$.

§4.3 Cylindrical Shell Problem

In [6] Newton presented several sets of results for an infinite cylindrical shell problem using the special-purpose two-dimensional code DPLPOT, but a direct comparison of his calculations with those of USA-STAGS-CFA could not be readily made. This is because his structural model included a damped oscillator whose properties were adjusted to simulate a neutrally bouyant shell with internal equipment. The oscillator, however, couples only to the $n = 1$ rigid-body mode of the shell. As USA-STAGS-CFA is not based upon modal superposition and could not easily emulate the oscillator action, Professor Newton kindly consented to rerun one of his cases without the oscillator.

The structural model used in this study consisted of one row of twelve STAGS 410-shell elements around half the circumference in order to take advantage of symmetry. The shell radius was 500 cm and the axial width was chosen as 130.9 cm so that the element aspect ratio was unity. The shell wall was of sandwich construction with 2.5-cm-thick face sheets separated by a massless core 29.1-cm-thick that was allowed to carry transverse shear only. The physical properties of the shell material correspond to structural steel. The values used were 7.83 gm cm^{-3} for the density, $2.1 \times 10^{12} \text{ gm cm}^{-1}\text{sec}^{-2}$ for Young's modulus, and 0.30 for Poisson's ratio. The behavior of the structure was constrained to be linear at all times.

The fluid-volume model consisted of 192 brick elements arranged in 16 concentric circular cylindrical layers about the shell; each layer is subdivided into twelve equal sectors subtending a 15° angle. The 12-element DAA boundary surrounds the fluid-volume mesh at a radius of 2500 cm. The intermediate radii for each successive layer increase in geometric proportion at a rate of 1.105823. The physical properties of the fluid represent sea water, with values of 1.024 gm cm^{-3} for the density ρ and $1.5 \times 10^5 \text{ cm sec}^{-1}$ for the speed of sound c .

The hydrostatic pressure was $10^7 \text{ gm cm}^{-1}\text{sec}^{-2}$ throughout the fluid volume. The peak magnitude of the step-exponential plane wave was $8 \times 10^7 \text{ gm cm}^{-1}\text{sec}^{-2}$ while the decay time was 5 milliseconds.

The time step used in the transient response analysis was .125 milliseconds (the Courant limit being .352 milliseconds) and the artificial damping coefficient β was taken as unity. The response calculation was carried for 160 steps out to a time of 20 milliseconds and cavitation was allowed to occur if the absolute pressure dropped below a value of zero.

Comparative results are shown in Figures 9 through 17. The solid lines represent the USA-STAGS-CFA calculations while the discrete symbols represent Newton's computations (which were provided at half-millisecond intervals). Figures 9, 10, and 11 show radial displacement histories at the initial point of contact of the wave on the shell, at 90° from the contact point, and at 180° on the back of the shell, respectively. Figures 12, 13, and 14 show radial velocities at the same locations while Figures 15, 16, and 17 show total pressures at those locations. In these plots the displacement and velocity responses have been rescaled so that the length measure is meters, while the pressure values have been multiplied by 10^{-7} so that they represent megapascals. Time is given in milliseconds.

As can be seen the correspondence is very good for the selected displacement and pressure histories, except for the displacement at 90° , which is more sensitive than those at 0° and 180° to discretization details and modal convergence problems. Although the USA-STAGS-CFA velocity responses contain oscillations that do not appear in Newton's solution, the responses agree quite well on the average, especially at 0° and 180° . (As explained in the Remark on page 4-8, these oscillations are due to discretization effects, and do not have physical significance.)

It should be mentioned that the early-time pressure peak of Figure 15 is a *real* effect that is masked in the DPLPOT results by the coarse output-sampling interval.

It is remarkable that such good correlation has been obtained even though there is a marked disparity in the discretization details. Newton used 31 modes for the structural response, and approximately 3000 two-dimensional fluid-volume elements of similar size to fill a rectangular region around a half cylinder model. Furthermore, his time step was one-fourth of that used in the USA-STAGS-CFA computations.

Although the structural response is of greatest interest in these studies, cavitation does occur in this problem and an idea of its extent can be gathered from Figures 18 and 19, which are fluid-pressure "snapshots" at 8 milliseconds. The location and shape of the cavitating region is roughly the same in both sets of computations; the region closes after 16 milliseconds.

The fact that structural responses agree quite well despite the use of a much coarser fluid model in the USA-STAGS-CFA computations augurs well for the applicability of this new modeling capability to large three-dimensional underwater-shock problems.

Remark. A more refined USA-STAGS-CFA analysis of this problem was carried out after the initial draft of this report was prepared. The spatial grid was halved as well as the time step, resulting in a 320-step calculation involving 768 fluid-volume elements and 24 structural elements. The velocity oscillations of Figures 12 through 14 became hardly noticeable, which shows them as a "coarse grid" effect. The displacement and velocity histories at $\theta = 90^\circ$ displayed better correlation with Newton's results, while agreement for the other sample histories remained excellent.

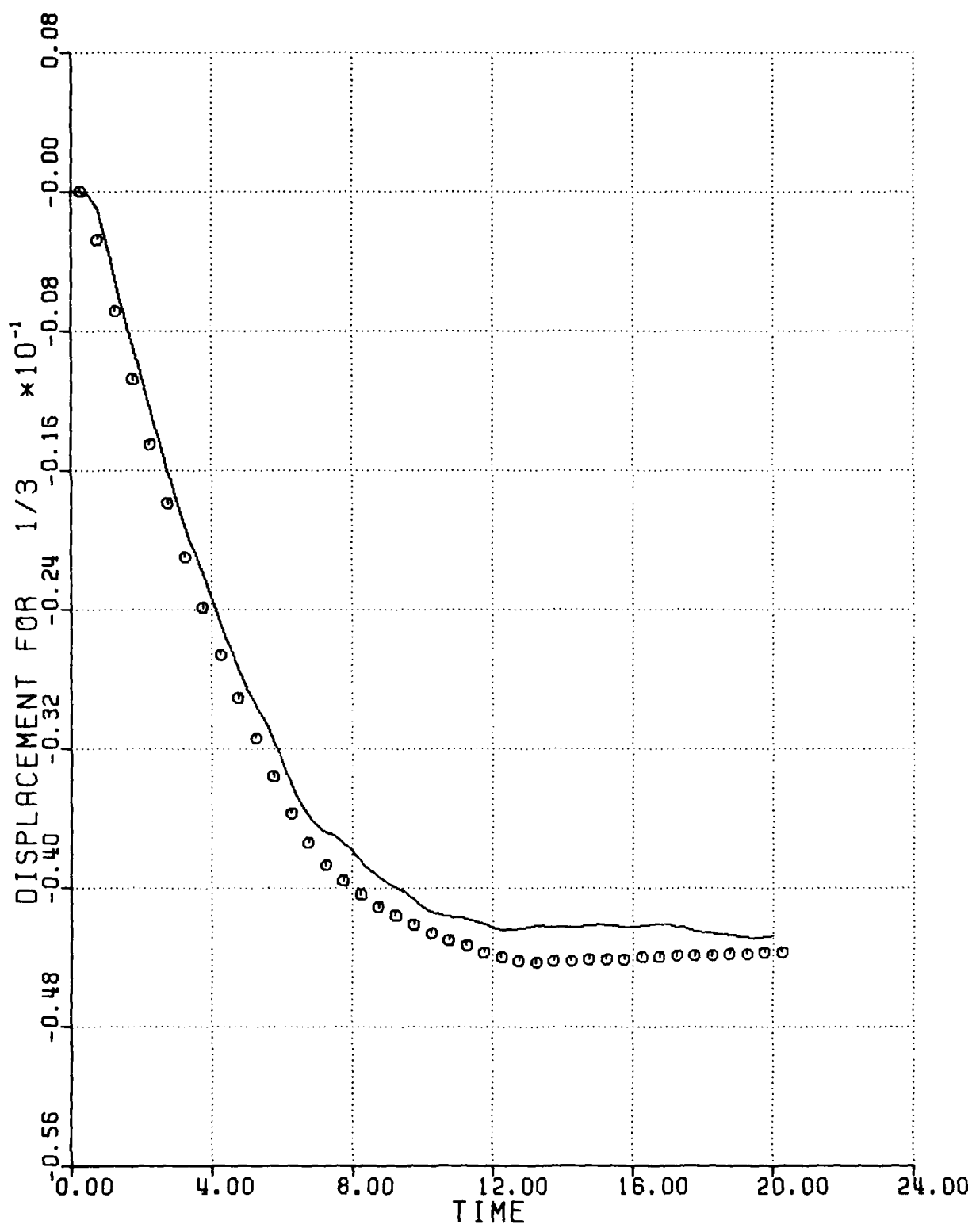


Figure 9 Radial displacement of cylindrical shell, $\theta = 0^\circ$.

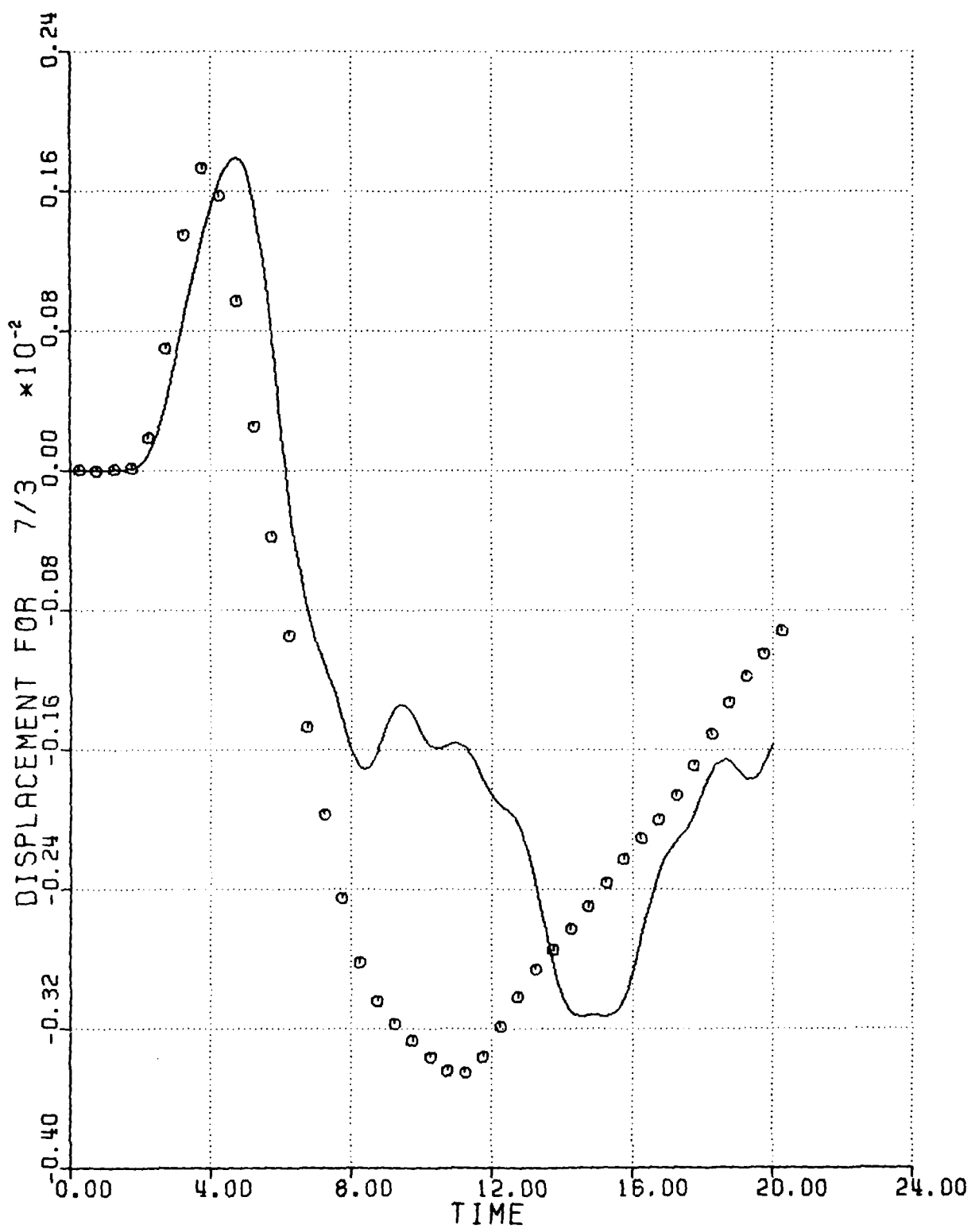


Figure 10 Radial displacement of cylindrical shell, $\theta = 90^\circ$.

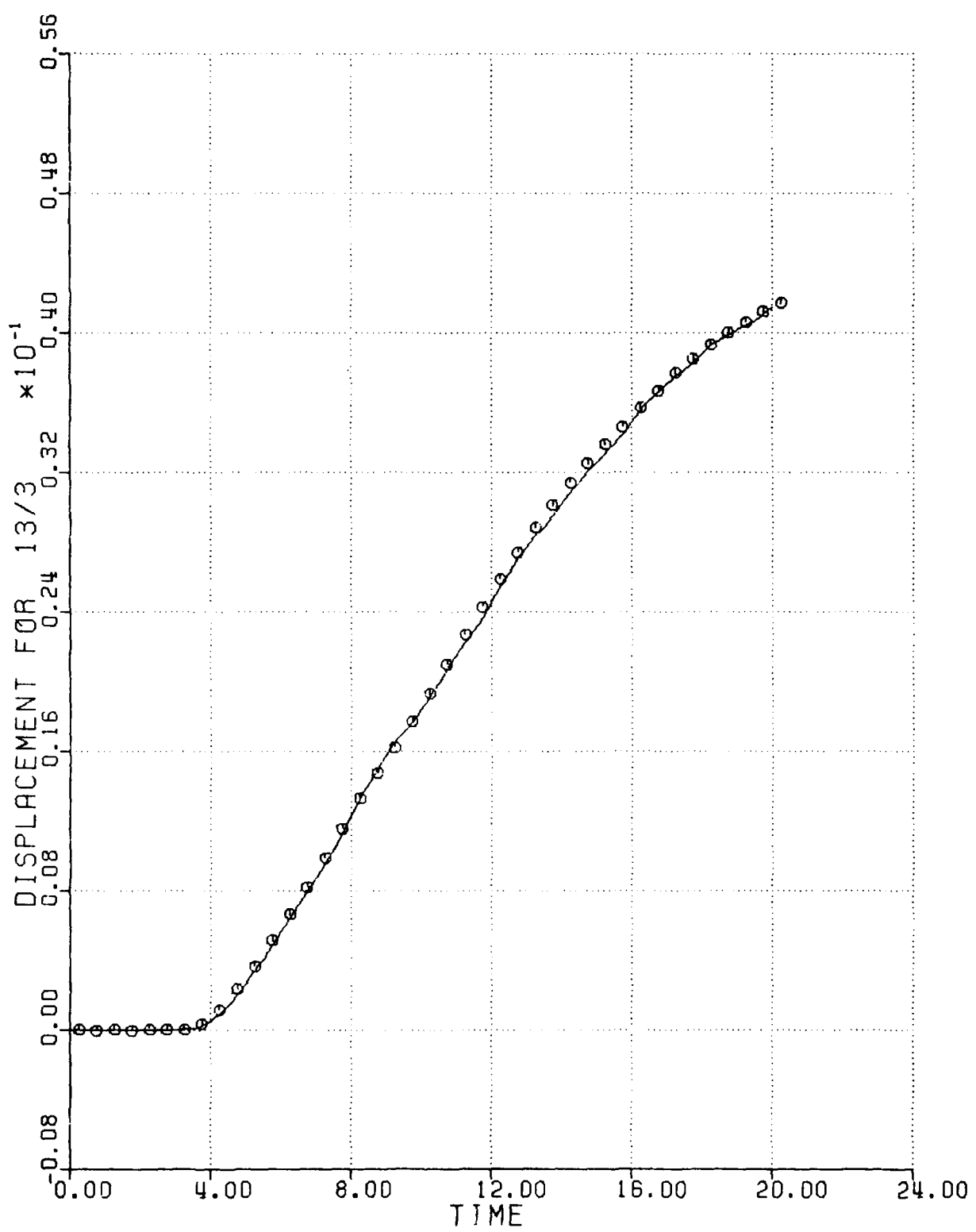


Figure 11 Radial displacement of cylindrical shell, $\theta = 180^\circ$.

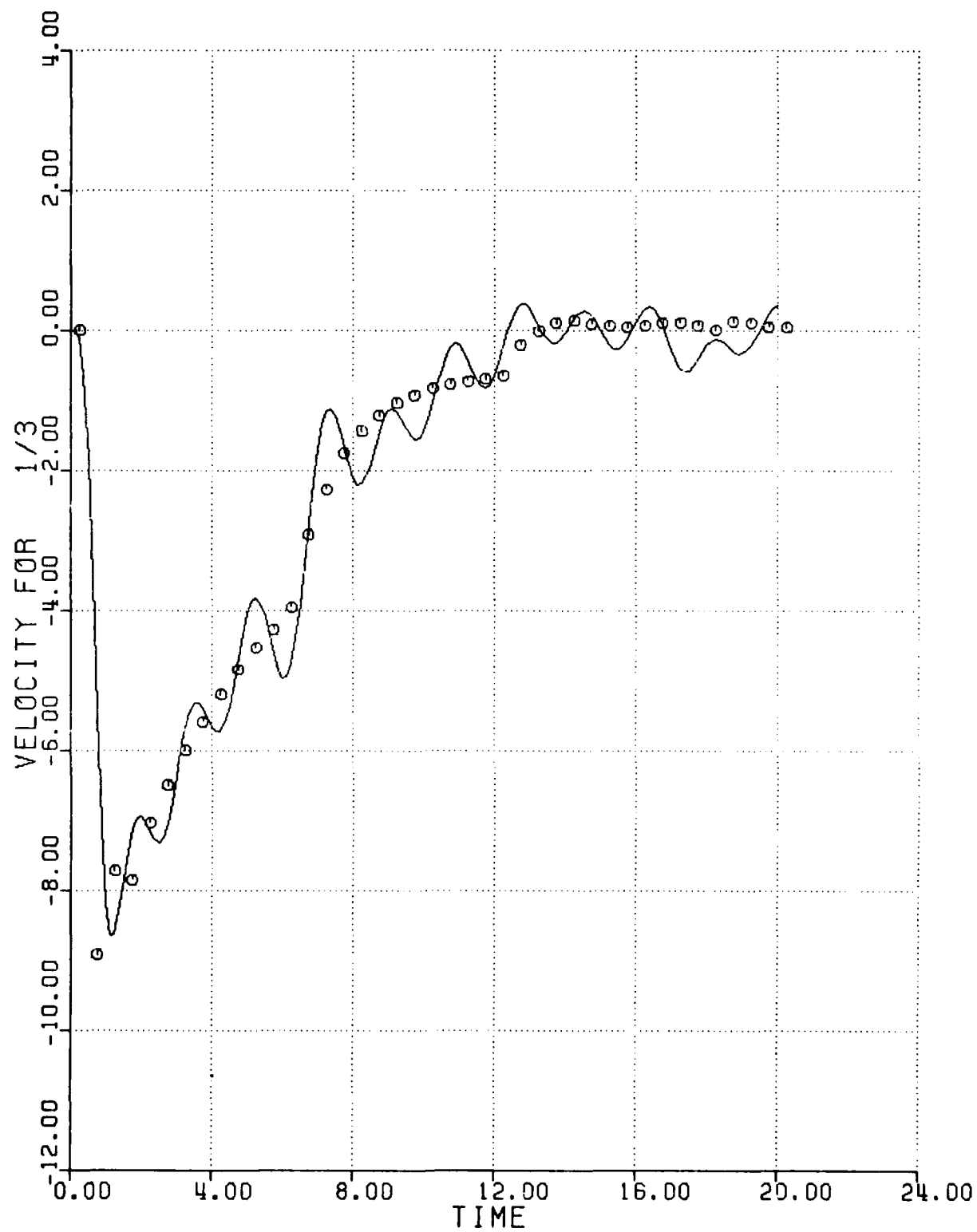


Figure 12 Radial velocity of cylindrical shell, $\theta = 0^\circ$.

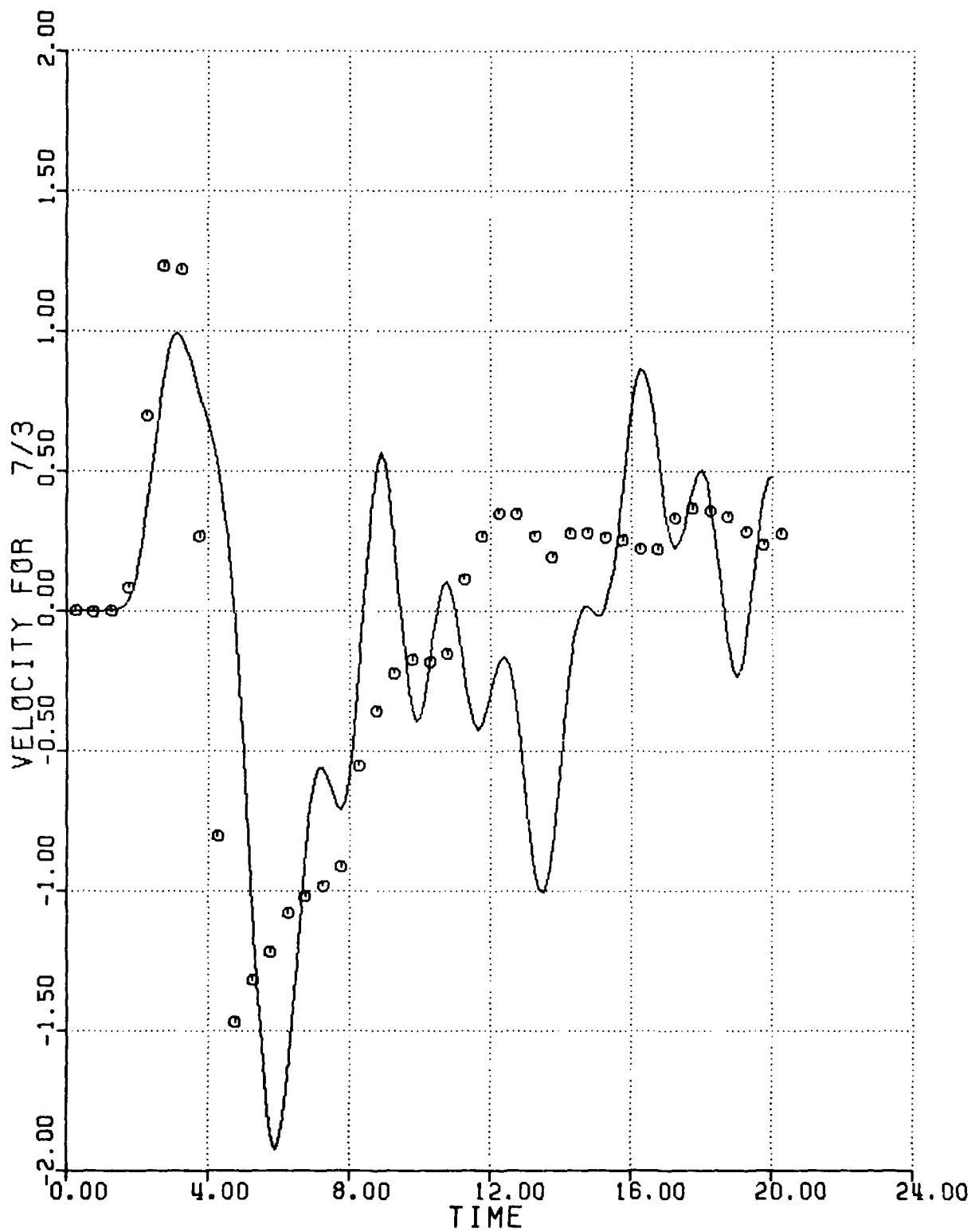


Figure 13 Radial velocity of cylindrical shell, $\theta = 90^\circ$.

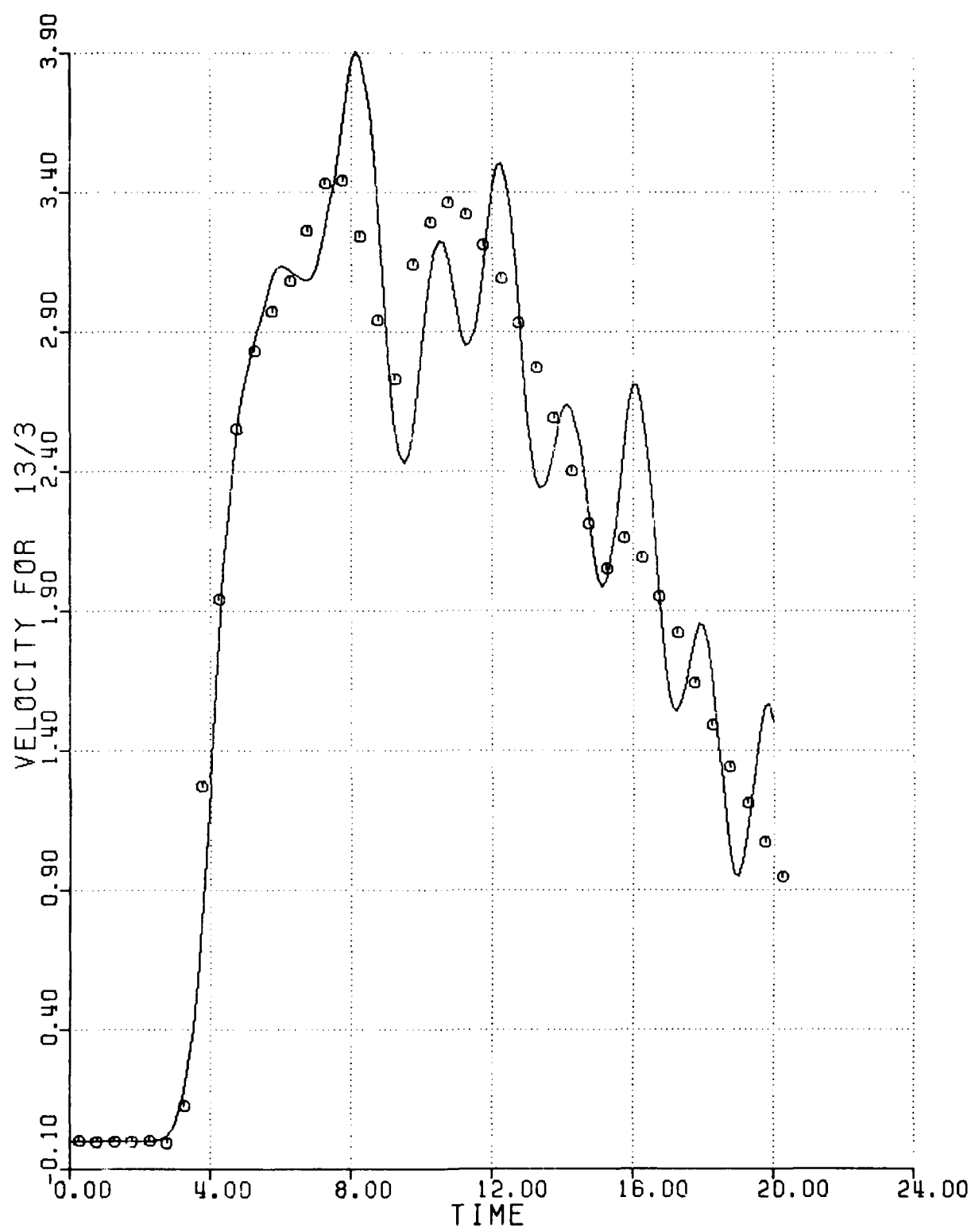


Figure 14 Radial velocity of cylindrical shell, $\theta = 180^\circ$.

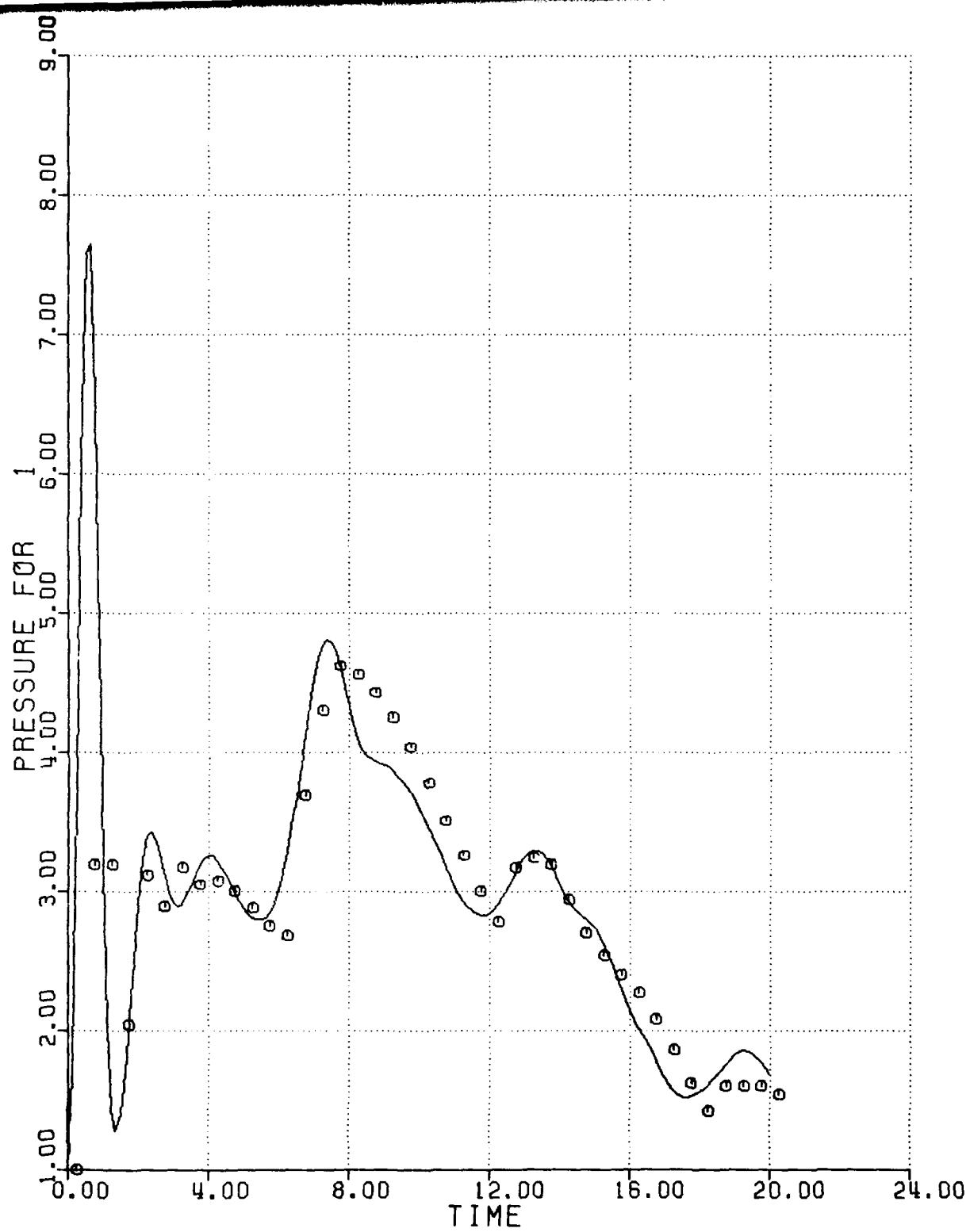


Figure 15 Total pressure on cylindrical shell, $\theta = 0^\circ$.

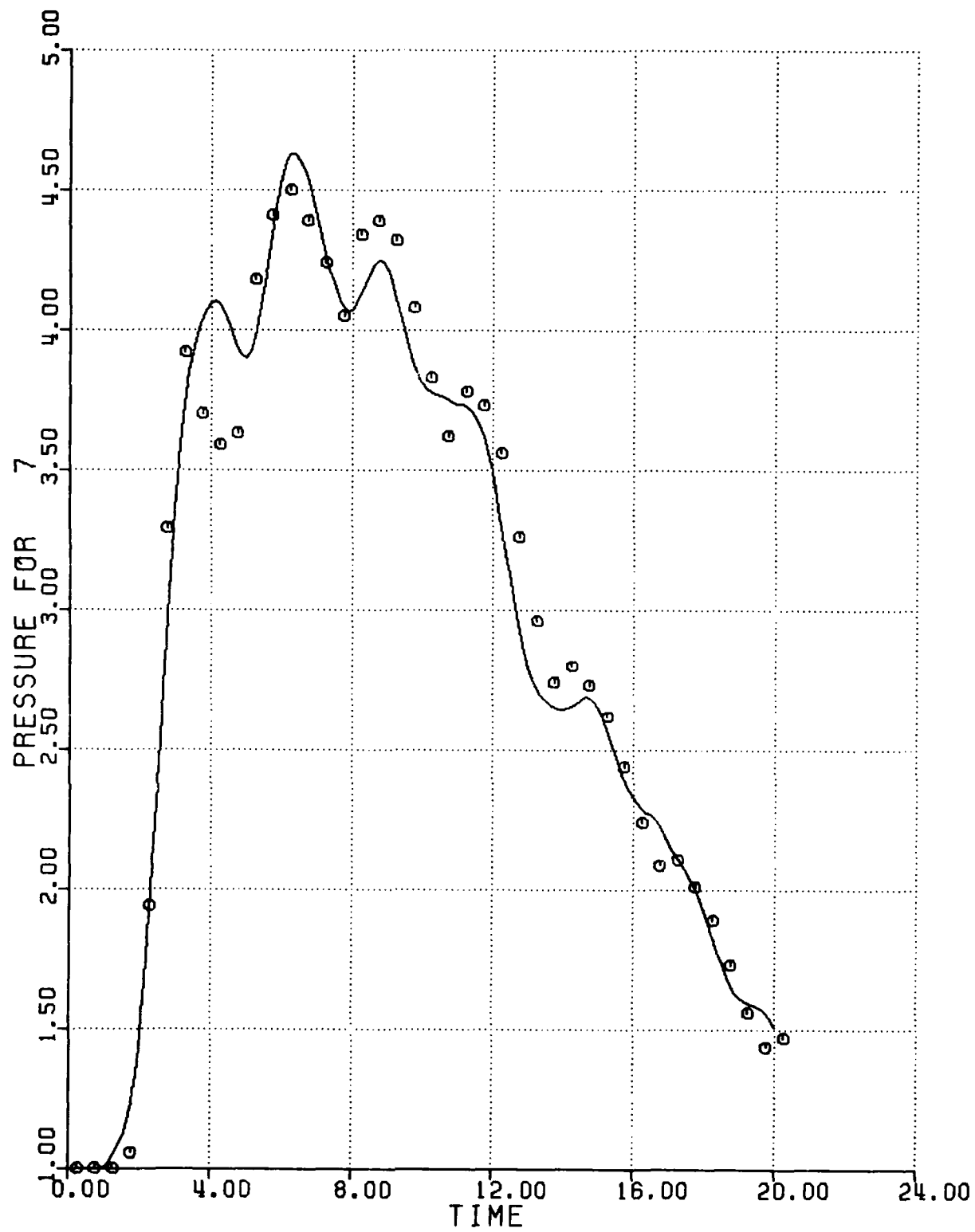


Figure 16 Total pressure on cylindrical shell, $\theta = 90^\circ$.

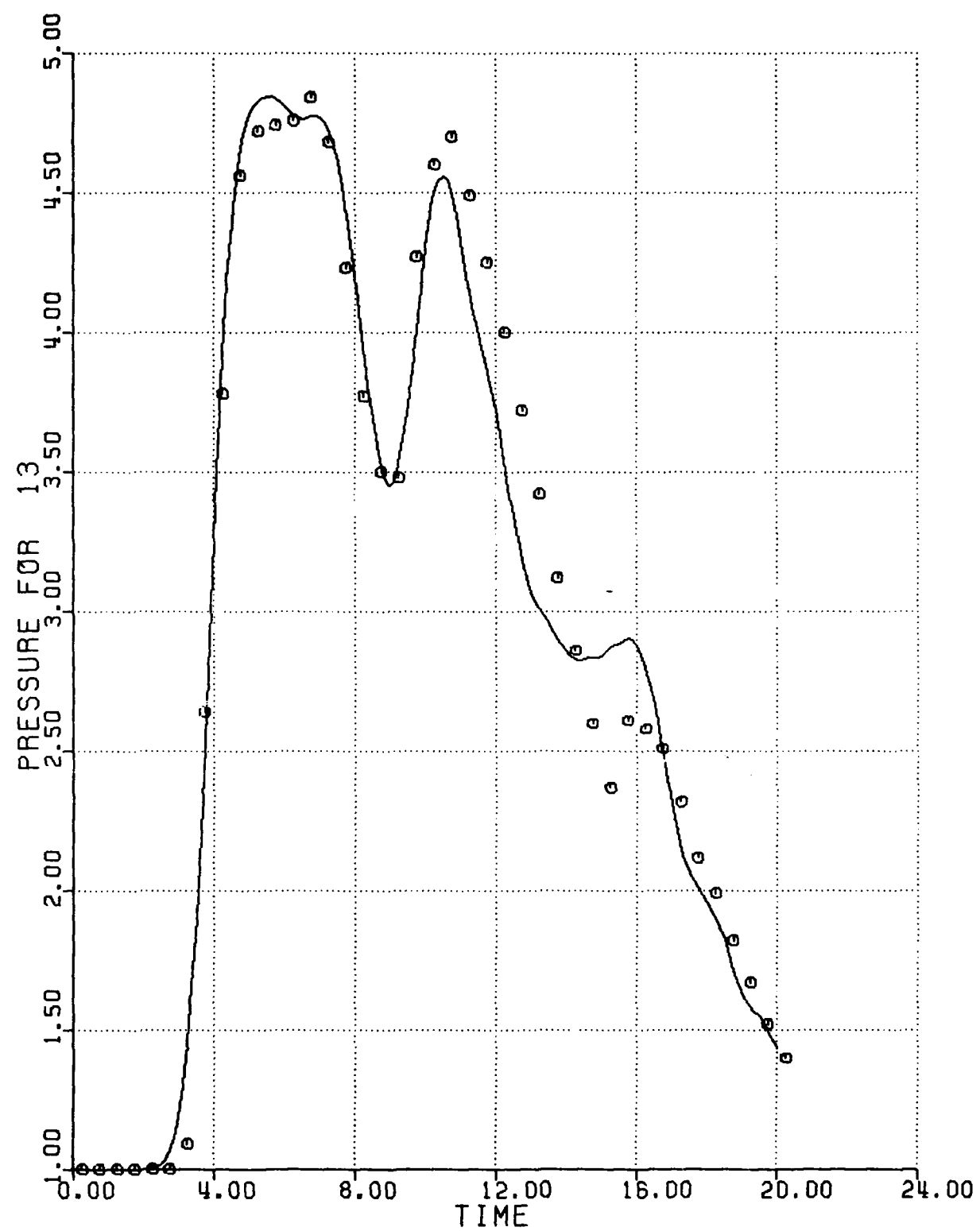


Figure 17 Total pressure on cylindrical shell, $\theta = 180^\circ$.

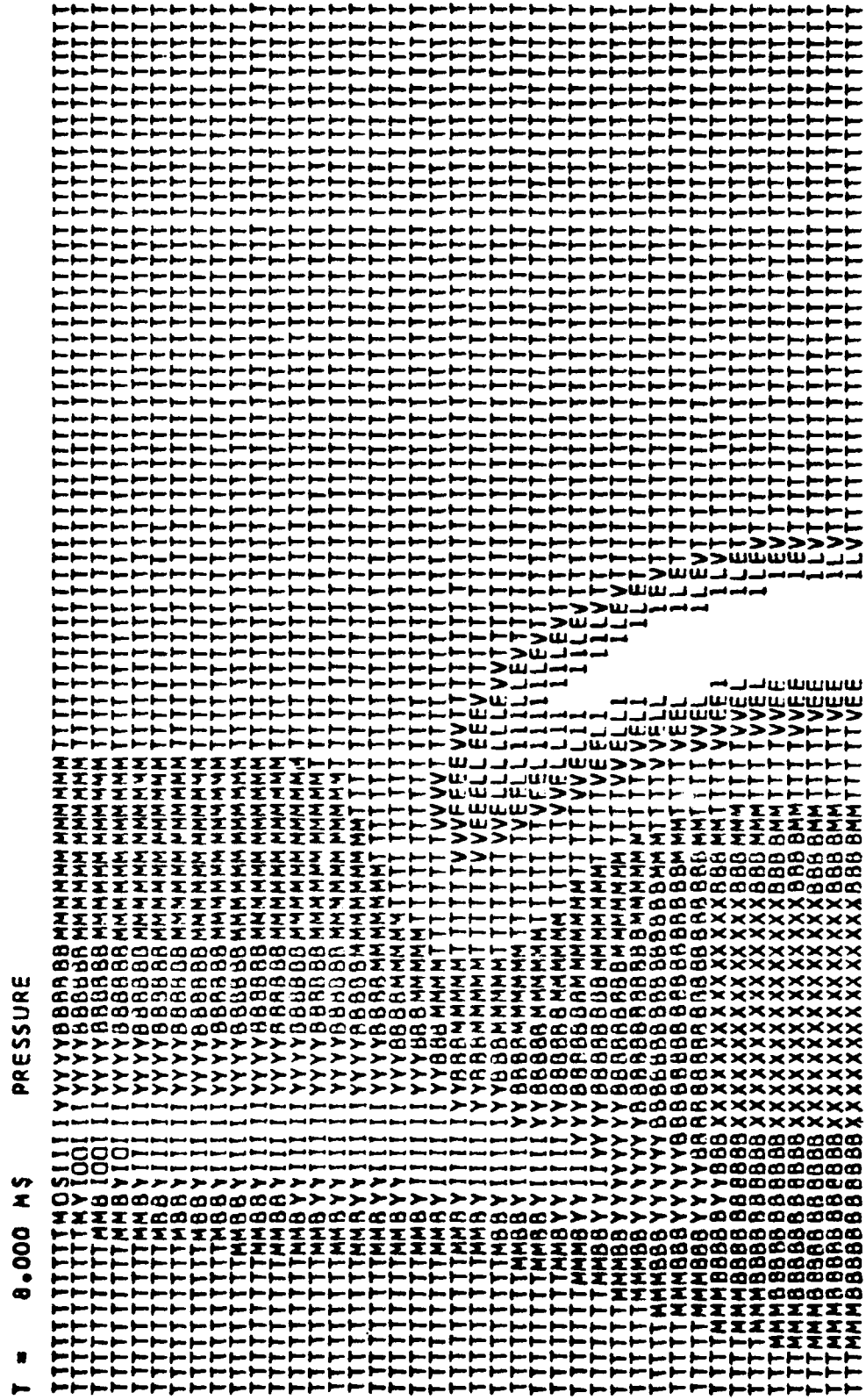


Figure 18 Map of cavitation zone at $t=8 \text{ ms}$, DPLPOT.

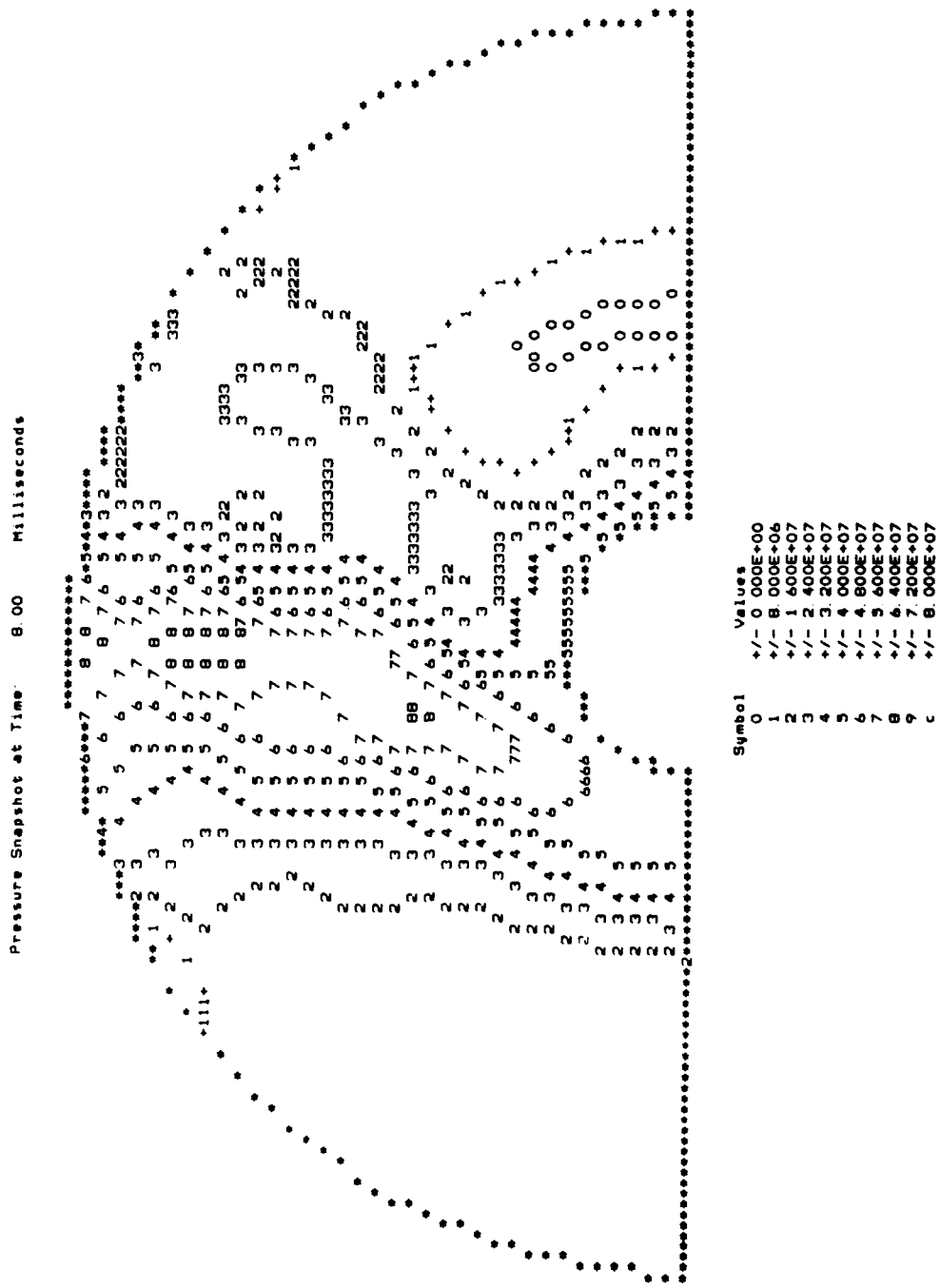


Figure 19 Map of cavitation zone at t=8 ms, USA-STAGS-CFA.

REFERENCES

- [1] J. A. DeRuntz and F. A. Brogan, "Underwater Shock Analysis of Non-linear Structures, A Reference Manual for the USA-STAGS Code," DNA 5545F, Defense Nuclear Agency, Washington, D.C., December 1980.
- [2] T. L. Geers, "Residual Potential and Approximate Methods for Three-Dimensional Fluid-Structure Interaction Problems," *J. Acoust. Soc. Am.*, Vol. 49, No. 5, May 1971, pp. 1505-1510.
- [3] T. L. Geers, "Doubly Asymptotic Approximations for Transient Motions of Submerged Structures," *J. Acoust. Soc. Am.*, Vol. 64, No. 5, Nov. 1978, pp. 1500-1508.
- [4] R. E. Newton, "Effects of Cavitation on Underwater Shock Loading - Part I," NPS69-78-013, Naval Postgraduate School, Monterey, California, July 1978.
- [5] H. H. Bleich and I. S. Sandler, "Interaction between Structures and Bilinear Fluids," *Int. J. Solids Structures*, Vol. 6, 1970, pp. 617-639.
- [6] R. E. Newton, "Effects of Cavitation on Underwater Shock Loading - Plane Problem, Final Report," NPS-69-81-001, Naval Postgraduate School, Monterey, California, March 1981.
- [7] R. E. Newton, "Finite Element Analysis of Shock-Induced Cavitation," Preprint 80-110, ASCE Spring Convention, Portland, Oregon, April 1980.
- [8] K. C. Park, C. A. Felippa and J. A. DeRuntz, "Stabilization of Staggered Solution Procedures for Fluid-Structure Interaction Analysis," in *Computational Methods for Fluid-Structure Interaction Problems*, AMD-Vol. 26, ASME, New York, 1977, pp. 95-124.

DISTRIBUTION LIST

DEPARTMENT OF DEFENSE

Defense Advanced Rsch Proj Agency
ATTN: TIO

Defense Intelligence Agency

ATTN: DB-4C2
ATTN: DB-4C2, C. Wiehle
ATTN: DT-1C
ATTN: DT-2
ATTN: RTS-2A, Tech Lib
ATTN: DB-4C3
ATTN: DB-4C, Rsch, Phys Vuin Br
ATTN: DB-4C1

Defense Nuclear Agency

ATTN: SPSS
ATTN: STSP
4 cy ATTN: TITL

Defense Technical Information Center
12 cy ATTN: DD

Field Command

Defense Nuclear Agency, Det 1
Lawrence Livermore Lab
ATTN: FC-1

Field Command

Defense Nuclear Agency
ATTN: FCPR
ATTN: FCT
ATTN: FCTX
ATTN: FCTT, G. Ganong
ATTN: FCTT, W. Summa
ATTN: FCTXE

Field Command Test Directorate
ATTN: FCTC

Joint Strat Tgt Planning Staff

ATTN: NRI-STINFO Library
ATTN: JLA, Threat Applications Div
ATTN: JLTw, Rautenberg
ATTN: JLTw-2
ATTN: DOXT
ATTN: XPFS

Under Secy of Def for Rsch & Engrg
ATTN: Strategic & Space Sys (OS)

DEPARTMENT OF THE ARMY

BMD Advanced Technology Center
ATTN: ICRDABH-X
ATTN: ATC-T

Chief of Engineers

ATTN: DAEN-RDL
ATTN: DAEN-MPE-T

Dep Ch of Staff for Rsch Dev & Acq
ATTN: DAMA

Engineer Studies Center
ATTN: DAEN-FES, LTC Hatch

DEPARTMENT OF THE ARMY (Continued)

Harry Diamond Laboratories
ATTN: DELHD-NW-P
ATTN: DELHD-TA-L

US Army Concepts Analysis Agency
ATTN: CSSA-ADL

US Army Engineer Ctr & Ft Belvoir
ATTN: ATZA-DTE-ADM

US Army Engineer School
ATTN: ATZA-CDC

US Army Engr Waterways Exper Station
ATTN: R. Whalin
ATTN: WESSE
ATTN: WESSD, J. Jackson
ATTN: J. Strange
ATTN: J. Zelasko
ATTN: F. Brown
ATTN: Library
ATTN: WESSA, W. Flathau
ATTN: WESSS, J. Ballard

US Army Foreign Science & Tech Ctr
ATTN: DRXST-SD

US Army Material & Mechanics Rsch Ctr
ATTN: DRXMR, J. Mescall
ATTN: Technical Library

US Army Material Dev & Readiness Cmd
ATTN: DRCDE-D, L. Flynn
ATTN: DRXAM-TL

US Army War College
ATTN: Library

USA Military Academy
ATTN: Document Library

USA Missile Command
ATTN: Documents Section
ATTN: DRSMI-RH

DEPARTMENT OF THE NAVY

David Taylor Naval Ship R&D Ctr
ATTN: Code L42-3
ATTN: Code 1700, W. Murray
ATTN: Code 1844
ATTN: Code 177, E. Palmer
ATTN: Code 172
ATTN: Code 1770.1
ATTN: Code 174
ATTN: Code 2740
ATTN: Code 1740.4
ATTN: Code 1740, R. Short
ATTN: Code 173
ATTN: Code 11
ATTN: Code 1740.5
ATTN: Code 1740.6
ATTN: Code 1740.1

DEPARTMENT OF THE NAVY (Continued)

Naval Civil Engineering Laboratory
ATTN: Code L51, J. Crawford

Naval Coastal Systems Laboratory
ATTN: Code 741

Naval Explosive Ord Disposal Fac
ATTN: Code 504, J. Petrousky

Naval Facilities Engineering Command
ATTN: Code 04B

Naval Material Command
ATTN: MAT 08T-22

Naval Ocean Systems Center
ATTN: Code 013, E. Cooper
ATTN: Code 4471

Naval Postgraduate School
ATTN: Code 69NE
ATTN: Code 1424 Library
ATTN: Code 69SG, Y. Shin

Naval Research Laboratory
ATTN: Code 8403, R. Belsham
ATTN: Code 8440, G. O'Hara
ATTN: Code 6380
ATTN: Code 8100
ATTN: Code 8301
ATTN: Code 8406
ATTN: Code 2627
ATTN: Code 8445
ATTN: Code 8404, H. Pusey

Naval Sea Systems Command
ATTN: SEA-08
ATTN: SEA-55X1
ATTN: SEA-033
ATTN: SEA-06J, R. Lane
ATTN: SEA-09G53
ATTN: SEA-9931G
ATTN: SEA-323
ATTN: SEA-0351

Naval Surface Weapons Center
ATTN: Code F34
ATTN: Code R13
ATTN: Code R10
ATTN: Code U401, M. Kleinerman
2 cy ATTN: Code R14
ATTN: Code F31
ATTN: Code R15

Naval Surface Weapons Center
ATTN: W. Wishard
ATTN: Tech Library & Info Svcs Br

Naval War College
ATTN: Code E-11

Naval Weapons Center
ATTN: Code 343, FKA6A2
ATTN: Code 266, C. Austin
ATTN: Code 3263, J. Bowen

Naval Weapons Support Center
ATTN: Code 70553, D. Moore

DEPARTMENT OF THE NAVY (Continued)

Naval Weapons Evaluation Facility
ATTN: G. Binns
ATTN: Code 10
ATTN: Code 210
ATTN: R. Hughes

New London Laboratory
ATTN: Code 4494, J. Patel
ATTN: Code 4492, J. Kalinowski

Newport Laboratory
ATTN: Code EM
ATTN: Code 363, P. Paranzino

Ofc of the Deputy Chief of Naval Ops
ATTN: OP 987
ATTN: NOP 982, Tac Air Srf & Ewdev Div
ATTN: NOP 981
ATTN: NOP 654, Strat Eval & Anal Br
ATTN: OP 9878
ATTN: OP 982E, M. Lenzini
ATTN: OP 957E
ATTN: NOP 953, Tac Readiness Div
ATTN: OP 37
ATTN: OP 225
ATTN: OP 03EG
ATTN: OP 21
ATTN: NOP 951, ASW Div
ATTN: OP 605D5
ATTN: OP 981N1
ATTN: OP 223

Office of Naval Research
ATTN: Code 474, N. Perrone

Strategic Systems Project Office
ATTN: NSP-272
ATTN: NSP-43
ATTN: NSP-273

DEPARTMENT OF THE AIR FORCE

Air Force Institute of Technology
ATTN: Commander
ATTN: Library

Air Force Systems Command
ATTN: DLW

Air Force Weapons Laboratory
ATTN: NTES-G, S. Melzer
ATTN: NTE, M. Plamondon
ATTN: NTES-C, R. Henny
ATTN: SUL
ATTN: NTED

Assistant Chief of Staff
Intelligence
ATTN: IN

Ballistic Missile Office
ATTN: DEB

Deputy Chief of Staff
Research, Development, & Acq
ATTN: AFRDOI
ATTN: R. Steere

DEPARTMENT OF THE AIR FORCE (Continued)

Deputy Chief of Staff
Logistics & Engineering
ATTN: LEEE

Foreign Technology Division
ATTN: NIIS Library
ATTN: TQTD
ATTN: SDBG
ATTN: SDBF, S. Spring

Rome Air Development Center
ATTN: RBES, R. Mair
ATTN: Commander
ATTN: TSLD

Strategic Air Command
ATTN: NRI-STINFO Library

OTHER GOVERNMENT AGENCIES

Central Intelligence Agency
ATTN: OSWR/NED
ATTN: OSR/SE/F

NASA
ATTN: F. Nichols
ATTN: R. Jackson

DEPARTMENT OF ENERGY CONTRACTORS

University of California
Lawrence Livermore National Lab
ATTN: S. Erickson

Los Alamos National Laboratory
ATTN: R. Whitaker
ATTN: MS 530, G. Spillman
ATTN: Reports Library
ATTN: MS 634, T. Dowler
ATTN: R. Sanford
ATTN: MS 670, J. Hopkins

Sandia National Lab
ATTN: Tech Lib, 3141
ATTN: L. Vortman

Sandia National Labs, Livermore
ATTN: Library & Security Classification Div

DEPARTMENT OF DEFENSE CONTRACTORS

Applied Research Associates, Inc
ATTN: D. Piepenburg

Applied Research Associates, Inc
ATTN: B. Frank

BDM Corp
ATTN: T. Neighbors
ATTN: A. Lavagnino
ATTN: Corporate Library

California Institute of Technology
ATTN: T. Ahrens

Columbia University
ATTN: H. Bleich
ATTN: F. DiMaggio

DEPARTMENT OF DEFENSE CONTRACTORS (Continued)

California Research & Technology, Inc
ATTN: S. Schuster
ATTN: K. Kreyenhagen
ATTN: M. Rosenblatt
ATTN: Library

University of Denver
ATTN: Sec Officer for J. Wisotski

Electric Power Research Institute
ATTN: G. Sliter

Electro-Mech Systems, Inc
ATTN: R. Shunk

General Dynamics Corp
ATTN: J. Mador
ATTN: J. Miller
ATTN: M. Pakstys

Kaman AviDyne
ATTN: R. Ruetenik
ATTN: G. Zartarian
ATTN: Library
ATTN: N. Hobbs

Kaman Sciences Corp
ATTN: Library
ATTN: F. Shelton

Kaman Sciences Corp
ATTN: D. Sachs

Kaman Tempo
ATTN: DASIAC

Karagozian and Case
ATTN: J. Karagozian

Lockheed Missiles & Space Co, Inc
ATTN: Technical Information Center
ATTN: T. Geers
ATTN: B. Almroth
4 cy ATTN: C. Felippa
4 cy ATTN: J. DeRuntz

Lockheed Missiles & Spaces Co, Inc
ATTN: TIC-Library

M & T Company
ATTN: D. McNaught

McDonnell Douglas Corp
ATTN: R. Halprin

NKF Engineering Associates, Inc
ATTN: R. Belsheim

Pacific-Sierra Research Corp
ATTN: H. Brode, Chairman SAGE

Pacifica Technology
ATTN: A. Kushner
ATTN: R. Bjork
ATTN: G. Kent

Physics Applications, Inc
ATTN: C. Vincent

DEPARTMENT OF DEFENSE CONTRACTORS (Continued)

Physics International Co
ATTN: L. Behrmann
ATTN: F. Sauer
ATTN: J. Thomsen
ATTN: E. Moore
ATTN: Technical Library

S-CUBED

ATTN: T. Cherry
ATTN: R. Sedgewick
ATTN: D. Grine
ATTN: T. Riney
ATTN: Library
ATTN: K. Pyatt
ATTN: T. McKinley

Science Applications, Inc
ATTN: Technical Library

Southwest Research Institute
ATTN: A. Wenzel
ATTN: W. Baker

SRI International
ATTN: G. Abrahamson
ATTN: W. Wilkinson
ATTN: A. Florence

Westinghouse Electric Corp
ATTN: MS/ED-2, D. Bolton

DEPARTMENT OF DEFENSE CONTRACTORS (Continued)

Teledyne Brown Engineering
ATTN: J. Ravenscraft

Tetra Tech, Inc
ATTN: L. Hwang

TRW Electronics & Defense Sector
ATTN: P. Bhuta

ATTN: A. Feldman
ATTN: N. Lipner
ATTN: Technical Information Center
ATTN: D. Jortner
ATTN: B. Sussholtz

TRW Electronics & Defense Sector
ATTN: P. Dai
ATTN: F. Pieper
ATTN: E. Wong
ATTN: G. Hulcher

Weidlinger Assoc, Consulting Engrg
ATTN: J. McCormick
ATTN: M. Baron

Weidlinger Associates
ATTN: J. Isenberg